A window in the course of alkaline magma differentiation conducive to immiscible REE-rich carbonatites

Zineb Nabyl, Malcolm Massuyeau, Fabrice Gaillard, Johann Tuduri, Giada Iacono-Marziano, Grégory Rogerie, Emmanuel Le Trong, Ida Di Carlo, Jérémie Melleton, Laurent Bailly

Journal Pre-proofs

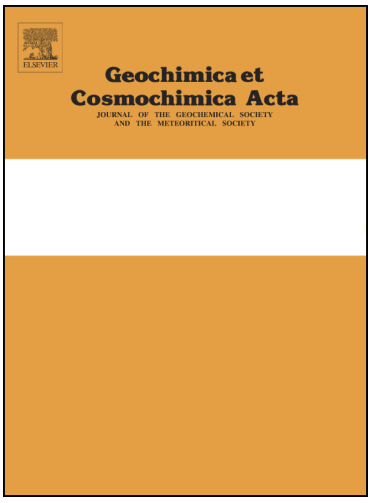

A window in the course of alkaline magma differentiation conducive to immiscible REE-rich carbonatites

Zineb Nabyl, Malcolm Massuyeau, Fabrice Gaillard, Johann Tuduri, Giada Iacono-Marziano, Grégory Rogerie, Emmanuel Le Trong, Ida Di Carlo, Jérémie Melleton, Laurent Bailly

PII: S0016-7037(20)30235-0
DOI: https://doi.org/10.1016/j.gca.2020.04.008
Reference: GCA 11731

To appear in: *Geochimica et Cosmochimica Acta*

Received Date: 23 July 2019
Revised Date: 3 April 2020
Accepted Date: 7 April 2020

Please cite this article as: Nabyl, Z., Massuyeau, M., Gaillard, F., Tuduri, J., Iacono-Marziano, G., Rogerie, G., Le Trong, E., Di Carlo, I., Melleton, J., Bailly, L., A window in the course of alkaline magma differentiation conducive to immiscible REE-rich carbonatites, *Geochimica et Cosmochimica Acta* (2020), doi: https://doi.org/10.1016/j.gca.2020.04.008

A window in the course of alkaline magma differentiation conducive to immiscible REE-rich carbonatites

Zineb Nabyl[a,*], Malcolm Massuyeau[b,c], Fabrice Gaillard[a], Johann Tuduri[d], Giada Iacono-Marziano[a], Grégory Rogerie[a], Emmanuel Le Trong[a], Ida Di Carlo[a], Jérémie Melleton[d], Laurent Bailly[d]

[a]ISTO, UMR 7327, Université d'Orléans, CNRS, BRGM, F-45071 Orléans, France
[b] Deep and Early Earth Processes (DEEP) Research Group, Department of Geology, University of Johannesburg, 2006 Auckland Park, South Africa
[c]Present adress: Institut für Mineralogie, University of Münster, D-48149 Münster, Germany
[d]BRGM, F-45060 Orléans, France

[*]Corresponding author at: ISTO, UMR 7327, Université d'Orléans, CNRS, BRGM, F-45071 Orléans, France
Email address: zineb.nabyl@univ-orleans.fr or zineb.nabyl@gmail.com (Z.Nabyl)

Abstract

Rare earth element (REE) enrichments in carbonatites are often described as resulting from late magmatic-hydrothermal or supergene processes. However, magmatic pre-enrichment linked to the igneous processes at the origin of carbonatites are likely to contribute to the REE fertilisation. Experimental constraints reveals that immiscibility processes between carbonate and silicate melts can lead to both REE enrichments and depletions in carbonatites making the magmatic processes controlling REE enrichments unclear.

We link REE contents of carbonatites to the magmatic stage at which carbonatites are separated from silicate magma in their course of differentiation. We present results of experiments made at pressure and temperature conditions of alkaline magmas and associated carbonatites differentiation (0.2 to 1.5 GPa; 725 to 975 °C; FMQ to FMQ +2.5), simultaneously addressing crystal fractionation of alkaline magmas and immiscibility between carbonate (calcio-carbonate type) and silicate melts (nephelinite to phonolite type). The experimental data shows that the degree of differentiation, controlling the chemical composition of alkaline melts, is a key factor ruling the REE concentration of the coexisting immiscible carbonate melts. In order to predict carbonate melt REE enrichments during alkaline magma differentiation, we performed a parameterisation of experimental data on immiscible silicate and carbonate melts, based exclusively on the silica content, the alumina saturation index and the alkali/alkaline-earth elements ratio of silicate melts. This parameterisation is applied to more than 1600 geochemical data of silicate magmas from various alkaline provinces (East African Rift, Canary and Cape Verde Islands) and show that REE concentrations of their potential coeval carbonatite melts can reach concentration ranges similar to those of highly REE enriched carbonatites ($\sum$REE > 30 000 ppm) by immiscibility with phonolitic/phono-trachytic melt compositions, while more primitive alkaline magmas can only be immiscible with carbonatites that are not significantly enriched in REE.

1. INTRODUCTION

Magmatic processes are believed to be at the origin of concentrations of many elements (e.g., Ni, Co, Pt, Pd, Au, Mo, Cu, Sn, Li, Zr, Nb, Ta, rare earth elements) yielding most of the giant ore deposits (Černý et al., 2005; Naldrett, 2010; Botcharnikov et al., 2011; Wilkinson, 2013; Linnen et al., 2014; Dostal, 2016; Song et al., 2016; Verplanck et al., 2016; Smith et al., 2016). Capturing the chain of processes involved in the formation of ore deposits thus requires the behaviour of metals in magmatic systems to be understood. Geochemical studies have related the behaviour of metal ions in magmatic systems, the oxidation state of the magma, the presence of volatiles and the molecular structure of both melt and coexisting crystals (Watson, 1976; Watson, 1979; Ponader and Brown, 1989a; Blundy and Wood, 2003; Mysen, 2004; Naldrett, 2010; Botcharnikov et al., 2011; Davidson et al., 2013; Linnen et al., 2014; Duc-Tin and Keppler, 2015; Song et al., 2016; Maimaiti et al., 2019). Among these metals in magmatic systems, the rare earth elements (REE) usually behave incompatible during magmatic differentiation (Schilling and Winchester, 1967; Loubet et al., 1972; Henderson, 1984; Nelson et al., 1988; McLennan and Taylor, 2012; Chakhmouradian and Zaitsev, 2012), i.e., they tend to remain in the residual silicate liquid and are therefore unlikely to form ore deposits. REE are relatively abundant in CO_2-rich magma, e.g., carbonatite and alkaline magma (Nelson et al., 1988; Green and Wallace, 1988; Chakhmouradian and Zaitsev, 2012; Verplanck et al., 2016), being strongly depolymerised liquids (Moussallam et al., 2016) and whose formation is related to the enigmatic deep carbon cycle (Rudnick et al., 1993; Tappe et al., 2017). REE-deposits associated to such magmatism remain very rare and capturing the processes that can concentrate REE in these CO_2-rich magma therefore constitute a major scientific objective (Nelson et al., 1988; Verplanck et al., 2016).

Carbonatites are igneous rocks composed of > 50 modal % primary carbonate minerals and less than 20 weight % (wt%) SiO_2 (Le Bas, 1981; Le Maitre et al., 2005). Carbonatites are generally enriched in REE compared to other igneous rocks (Loubet et al., 1972; Nelson et al., 1988; Woolley and Kempe, 1989), although their REE concentrations vary by two order of magnitudes ($\sum$REE around 0.05 to 4 wt%; Woolley and Kempe, 1989). More than 500 carbonatites are referenced worldwide (Woolley and Kjarsgaard, 2008) and only a few reach sufficient REE concentrations to warrant mining operation (Chakhmouradian and Wall, 2012; Chakhmouradian and Zaitsev, 2012; Wall, 2013; Verplanck et al., 2016; Smith et al., 2016). Late- to post-magmatic processes are usually suggested to produce the high concentrations, due to a combination of REE transport and deposition processes by fluids (Wall and Mariano, 1996; Yang et al., 2011; Chakhmouradian and Wall, 2012; Chakhmouradian and Zaitsev, 2012; Wall, 2014; Verplanck et al., 2016; Smith et al., 2016; Migdisov et al., 2016). On the other hand, primary REE fluoro-carbonates have also been suggested as magmatic phases (Wall and Mariano, 1996; Castor, 2008; Verplanck et al., 2016; Smith et al., 2016; Néron et al., 2018). While field descriptions (Castor, 2008; Verplanck et al., 2016; Broom-Fendley et al., 2016; Giebel et al., 2017) and thermodynamic modelling (Migdisov et al., 2016) leave no doubt as to the occurrence of hydrothermal

or supergene events in several carbonatite deposits, REE are likely to be primarily concentrated during the primary magmatic processes at the origin of carbonatite genesis (Chakhmouradian and Zaitsev, 2012; Song et al., 2016; Verplanck et al., 2016; Smith et al., 2016).

The origin of carbonatites is a matter of long-standing debate (Nelson et al., 1988; Woolley and Kjarsgaard, 2008; Jones et al., 2013; Smith et al., 2016) and is generally explained by three main hypotheses: i) carbonatites derive from primary magma produced by low degree of mantle partial melting (Wallace and Green, 1988; Rudnick et al., 1993; Bell and Simonetti, 2010; Dasgupta et al., 2013); ii) they are formed by extensive fractional crystallisation of a CO_2- bearing silicate parent magma (Lee and Wyllie, 1994; Mitchell, 2005; Tappe et al., 2017); iii) they are segregated from a silicate magma by immiscibility processes (Kjarsgaard and Hamilton, 1989; Lee and Wyllie, 1994; Veksler et al., 1998; Mitchell, 2005; Brooker and Kjarsgaard, 2011; Veksler et al., 2012; Martin et al., 2013). The first hypothesis relates the high REE contents of carbonatites to the low degree of mantle melting and the incompatible behaviour of REE (Rudnick et al., 1993; Mitchell, 2005; Bell and Simonetti, 2010; Doucelance et al., 2010; Smith et al., 2016), but very few occurrences of primary mantle carbonatite have been so far described (Doucelance et al., 2010; Schmidt and Weidendorfer, 2018). The immiscibility hypothesis is suggested by field evidences showing carbonatite and alkaline magma spatial associations (Kjarsgaard and Hamilton, 1989; Mitchell, 2005; Woolley and Kjarsgaard, 2008), and supported by experimental surveys (Kjarsgaard and Hamilton, 1989; Lee and Wyllie, 1994; Veksler et al., 1998; Brooker and Kjarsgaard, 2011; Veksler et al., 2012; Martin et al., 2013). A combination of hypothesis ii) and iii) has also been proposed, with the formation of a carbonate melt by immiscibility with a highly fractionated CO_2-rich alkaline silicate magma (Woolley and Kjarsgaard, 2008). The immiscibility hypothesis implying that carbonatite can segregate by liquid-liquid immiscibility at some stage in the alkaline magma differentiation course, is the most currently used to explain carbonatite genesis (Kjarsgaard and Hamilton, 1989; Weidendorfer et al., 2017).

Numerous experimental studies using both simplified synthetic and natural compositions have shown that immiscibility between carbonate and silicate melts can occur in a wide range of pressure and temperature (P-T) conditions, from the mantle to the crust (Lee and Wyllie, 1994; Kjarsgaard et al., 1995; Kjarsgaard, 1998; Veksler et al., 1998; Brooker and Kjarsgaard, 2011; Veksler et al., 2012; Martin et al., 2012; Martin et al., 2013; Massuyeau et al., 2015). The range of carbonate and silicate melt compositions subject at equilibrium to immiscibility remains however debated (Martin et al., 2013; Schmidt and Weidendorfer, 2018). A limited number of experimental studies (Hamilton et al., 1989; Veksler et al., 1998; Veksler et al., 2012; Martin et al., 2013) has focused on trace element partitioning between immiscible carbonate and silicate melts. The carbonate-silicate melt partition coefficients ($D_x^{CL/SL}$, with the element x) define the affinity of elements either for the carbonate liquid ($D_x^{CL/SL}>1$) or the silicate liquid ($D_x^{CL/SL}<1$). These experimental partition coefficients reveal surprisingly large variations of the REE behaviour during immiscibility, ranging from a moderate affinity for the silicate

melt ($D_x^{CL/SL} < 1$; Hamilton et al., 1989; Veksler et al., 1998; Veksler et al., 2012; Martin et al., 2013) to a strong affinity for the carbonate melt ($D_x^{CL/SL} > 1$; Hamilton et al., 1989; Martin et al., 2013). These contrasting REE behaviours during carbonate-silicate partitioning could be linked to the large range of REE contents in natural carbonatites (by two order of magnitude; Woolley and Kempe, 1989). However, no prevailing experimental parameter (P-T conditions, oxygen fugacity or experimental inconsistencies) has been identified to explain such large REE behaviour variations. Hamilton et al. (1989) proposed a pressure and temperature influence on REE partitioning between carbonate and silicate melts. The polymerisation of the silicate liquid has also been suggested to control these variations (Hamilton et al., 1989; Martin et al., 2013). However, silicate melt polymerisation, being usually addressed by the non-bridging-oxygen parameter (Mysen, 1990), does not take into account the CO_2 and the water contents of the melts (Moussallam et al., 2016). Noteworthy, the highest REE partition coefficients ($D_{REE}^{CL/SL}$) correspond to hydrous compositions (Martin et al., 2013) offering a sound link between REE enrichment and late-magmatic hydrothermal events. Nonetheless, such an effect of water has not been systematically characterised since, in the current experimental database, the water content of the silicate melt co-varies with other parameters (P-T conditions). Likewise, halogens and more specifically fluorine, are assumed to play an important role on REE behaviour (Ponader and Brown, 1989b; Keppler, 1993; Wall and Mariano, 1996; Veksler et al., 2005; Veksler et al., 2012; Chakhmouradian and Zaitsev, 2012; Aseri et al., 2015; Duc-Tin and Keppler, 2015; Song et al., 2016; Chebotarev et al., 2019). Indeed, halogens may occur in carbonatites as immiscible salt melts in melt inclusions (Panina and Motorina, 2008). Primary REE fluoro-carbonate minerals have also been recognised as magmatic phases by textural evidences (Wall and Mariano, 1996; Castor, 2008; Verplanck et al., 2016; Néron et al., 2018). Such occurrences suggest the special role of salt liquids (carbonate, phosphate, fluoride and chloride) in REE partitioning, which have been tested by a few experimental studies (Veksler et al., 2005; Song et al., 2016; Yang and Van Hinsberg, 2019).

This brief analysis reveals that a combination of melting, differentiation, and liquid-liquid immiscibility processes must contribute to the genesis of carbonatites. Most experimental studies on REE behaviour between carbonate and alkaline melts have however only focused on liquid-liquid immiscibility (Kjarsgaard et al., 1995; Kjarsgaard, 1998). This implies that the REE behaviour along the differentiation path of alkaline magma – carbonatite pairs have not been addressed yet.

We present experiments simulating the immiscibility between carbonate and silicate melts during crystal fractionation of alkaline silica-undersaturated magmas, in order to assess the parameters controlling carbonatite REE enrichments over the course of alkaline magma differentiation. Our experiments are performed at 725 to 975 °C and 0.2 to 1.5 GPa, to complete the pressure-temperature space of previous work (Freestone and Hamilton, 1980; Hamilton et al., 1989; Jones et al., 1995; Veksler et al., 1998; Veksler et al., 2012; Martin et al., 2013) in order to match the moderate pressure - temperature conditions of differentiation of alkaline magmas and associated carbonatites (Hamilton et al., 1989; Kjarsgaard et

al., 1995; Kjarsgaard, 1998; Martin et al., 2013), at fO_2 varying from FMQ to FMQ + 2.5 and with additional water, graphite, K and F in selected samples. We propose the parameterisation of carbonate melt REE enrichments by closer analysis of the silicate melt composition role during alkaline magma differentiation. This parameterisation highlights the occurrence of a carbonatite REE enrichments optimum along the differentiation course of alkaline magma.

2. METHODS

2.1 Starting materials

The starting material used for the experiments consisted of a mixture between synthetic hydrated nephelinite powder and synthetic calcite, in a ratio 90:10 respectively (bulk composition from Kjarsgaard, 1998). The nephelinite powder was made from the mixture of synthetic powders (SiO_2, TiO_2, Al_2O_3, Fe_2O_3, FeO, MnO_2, $Mg(OH)_2$, $CaCO_3$, Na_2CO_3, K_2CO_3, wollastonite, NaF, NaCl, $SrCO_3$, SrF_2, BaO, $BaCO_3$, Nb_2O_5), natural dolomite ($CaMg(CO_3)_2$) and apatite. The bulk composition is reported as Mix 8 in Table 1. For two samples, two supplementary starting materials were synthetised by mixing Mix 8 with pure K_2CO_3 in a ratio of 95:5 respectively (Mix 9, Table 1) and with pure CaF_2 in a ratio 97:3 (Mix 10), to investigate of potential effect of K and F in silicate and carbonate melt compositions. The starting materials are CO_2 and H_2O-rich (calculated concentrations of around 12 and 0.77 wt % respectively). In selected samples, the starting mix was doped in water and graphite (Table 2), the latter to create a more reduced environment and to check its effect on silicate and carbonate melt compositions. Each of the starting compositions was doped with 0.1 wt% ∑REE and Y, added in the form of oxides, elements or fluorides (La_2O_3, CeO_2, Pr_6O_{11}, Nd_2O_3, Sm_2O_3, Eu_2O_3, GdF_3, Tb, Dy_2O_3, HoF_3, Er_2O_3, Yb_2O_3, Lu, and Y_2O_3). All the synthetic powders were preserved in a dry oven at 120°C. Given the low concentration of REE, a good homogenisation was ensured by preparing about 15g of each starting composition. The powder was mixed in an agate mortar first by hand (20-30 minutes), and then by an automatic grinder with agate mortar and ball mill (30 minutes).

2.2 Experiments

34 experimental charges were synthetised using piston cylinders (for P>0.5 GPa) and internally heated pressure vessels (P<0.5 GPa) at the ISTO laboratory (Institut des Sciences de la Terre d'Orléans, France). The experimental pressures and temperatures ranged from 0.2 to 1.5 GPa and 725 to 975°C (Table 2). About 20mg of starting material was loaded into either Au capsules (diameter of 2.5-2.9 mm) or Au_{80}-Pd_{20} capsules for the experiments at higher pressure (0.8 and 1.5 GPa)

Piston-cylinder experiments were performed at 850, 925, 950 and 975°C, and 0.8 to 1.5 GPa during 5 days using end-loaded piston-cylinder devices. The capsules were inserted in an alumina tube, filled with a powdered mixture of 50% AlSiMag (mix of Al, Si and Mg) – 50% hematite and closed at the top and the bottom by two MgO-plugs. The hematite powder provide an oxidised environment and we

estimate the fO_2 of the experiments between FMQ and FMQ+2. Then the assemblage was loaded into a classical ¾-inch piston cylinder assembly, constituted of graphite, pyrex and talc cylinders. On top and bottom of the assembly, two steel-plugs surrounded by pyrophyllite were placed to maintain the assemblage and the thermocouple (B-type, $Pt_{94}Rh_6$-$Pt_{70}Rh_{30}$) localised on the top of the sample. For all experiments, melting and homogenisation of the bulk composition was ensured by first bringing the assemblage at a higher temperature than the final required temperature during 2 hours (1100°C for the experiment at 950-975°C, and 1000 °C for experiments at 925°C). The final temperature was then reached within a couple of minutes. Each experiment was ended by an isobaric quench, by switching off the electrical source of heating at constant pressure. Uncertainties are considered to be ±12°C for the temperature and ± 0.1 GPa for pressure (Dasgupta et al. (2004) and reference therein).

Internally heated pressure vessel experiments were performed at 725-825-925 °C and pressure of 0.2 and 0.4 GPa during 5 days at temperatures > 825°C, and three weeks for the experiment at lower temperature (Table 2). Capsules were pressurised using Ar-H_2 (0.1-0.5 MPa of H_2 for total pressures of 0.2 and 0.4 GPa) in order to vary fO_2 conditions. In experiments loaded with 0.1 MPa and 0.5 MPa of Ar-H_2, the fO_2 is estimated at NNO+2.1 and NNO+0.9 in the autoclave respectively (estimation from Gaillard et al., 2001), which is equivalent to FMQ+2.5 and FMQ+1.5 for the experiment P-T conditions (after Frost, 1991), at water activity equals to unity. The fO_2 truly prevailing in experimental charges being water under-saturated (Table 2) is estimated lowered by 0.5 log-units, that is to say, FMQ+2 and FMQ+1 respectively. The pressure is recorded by a transducer calibrated against a Heise Bourdon gauge with an accuracy of ± 2 MPa (Gaillard et al., 2001; Andújar et al., 2013). The experiments were performed in a double-winding molybdenum and kantal furnaces with near-isothermal conditions in the 2-3 cm long hotspot (Di Carlo et al., 2006). Two S-type thermocouples ($Pt_{90}Rh_{10}$; uncertainty of ± 5°C) were placed at the top and the bottom of the sample and indicated gradients < 2-3°C along the samples (Di Carlo et al., 2006; Andújar et al., 2013). In order to ensure the growth of large crystals all experiments were initiated by a high T stage (i.e., 1000°C), followed by a ramp forcing the dwell temperature to be reached within a few minutes. The capsules were placed in an alumina tube fixed in the furnace hotspot at the top by a thin Pt wire. A drop-technique was used to ensure fast isobaric quench (rate of ~100°C/s; Di Carlo et al., 2006).

2.3 SEM and Electron microprobe-analysis

After the experiments, the run products were cut in length and mounted in resin. All the samples were polished using ethanol instead of water to avoid the dissolution of carbonate phases. The polished samples have been observed with a Merlin Compact Zeiss electron microscope (15 kV), equipped with a micro-analyser system with a resolution of 129 eV (EDS Bruker-QUANTAX-XFlash6), to identify the phase assemblages in each sample and examine their textures.

Electron microprobe (EMP) analyses were conducted on carbonate and silicate phases, using a Cameca SXFive electron microprobe (Institut des Sciences de la Terre d'Orléans, France) equipped with a WDS detector. All the silicate and carbonate melt analyses were performed at 15kV and 6nA, using the larger possible beam sizes (from 10 to 70 µm depending on the silicate and carbonate melt zone sizes), in order to reduce Na-loss during analysis, and to sample the average composition of the carbonate blebs. For carbonate melt analyses, no major carbonate effect on absorption correction has been observed (CalcZAF software) for all elements. Standards used for calibration were albite, apatite, orthose, andradite, topaze, vanadinite, MgO, Al_2O_3, Fe_2O_3, $MnTiO_3$, Cr_2O_3, NbLi, $BaSO_4$, and $SrCO_3$. A double-check has been made on secondary standards (albite, andradite, olivine and orthose) to confirm the validity of all the analysis. The count time for peak and background were 10s for all the elements, expect for the Ba (20s) and the Sr (30s).

2.4 Laser ablation ICP-MS analysis

REE concentrations of the carbonate and the silicate melts were determined using two LA-ICP-MS (Laser Ablation Inductively Coupled Plasma Mass Spectrometry) facilities: the Thermo Element XR magnetic sector ICP-MS of the IRAMAT-CEB laboratory (CNRS, Orléans, France; He: 650 mL/min; Ar: 950 mL/min), and the Agilent 7500 CS quadrupole ICP-MS of the LMV laboratory (Clermont-Ferrand, France; He: 550 mL/min; N_2: 2mL/min; Ar: 850 mL/min). Both systems employ a 193 nm excimer laser system (laser Resonetics), coupled to the mass spectrometer with He flushing the ablation cell. The analysis were performed with a laser repetition rate of 2-4 Hz and an ablation energy of 1.5 - 4 mJ, for both the carbonate and the silicate melts. Silicate and carbonate phases were analysed with both spectrometers for one sample (sample T19_01; Table 2 and 4) and indicated similar REE concentrations. Silicate glasses were analysed with spot sizes of 15 to 100 µm, depending on the available analysable surface. We compared the concentrations obtained for the same glass using different spot sizes, without finding any significant differences. Because carbonate liquids are impossible to quench into glasses, carbonate blebs- i.e. carbonate liquids quenched in two interlayered microcrystalline carbonates- were more difficult to analyse. The analysis were adapted to their heterogeneous textures and performed at different beam sizes (15-80 µm), in order to ensure a good accuracy of their composition. The mean value and the reasonable associated standard deviation support the validity of all the analysis (Table 4). The following isotopes were analysed: ^{139}La, ^{140}Ce, ^{141}Pr, ^{146}Nd, ^{147}Sm, ^{153}Eu, ^{159}Tb, ^{163}Dy, ^{165}Ho, ^{166}Er, ^{172}Yb, ^{175}Lu, ^{89}Y, ^{55}Mn, ^{88}Sr, ^{137}Ba, ^{93}Nb, ^{197}Au and ^{105}Pd (to verify a possible contamination by capsule during experiment), ^{43}Ca, ^{44}Ca and ^{29}Si.

Data reduction has been performed using GLITTER4.4 software (Van Achterbergh et al., 2001) providing REE concentrations for both carbonate and silicate phases and analytical uncertainty for each analysis. All elements were quantified using the NIST 610 standard glass (Pearce et al., 1997) and a checking has been made with other standards: NIST 612 and BCR-2G natural basaltic glass (Pearce et al., 1997; Rocholl, 1998; Jochum et al., 2016). Standards were analysed at the same beam size, frequency

and energy ablation to check the accuracy of the analyses. The element that was used as internal reference is Ca, which is precisely determined by electron microprobe analyses in both the carbonate and the silicate phases. Glitter software also calculates the analytical uncertainty (the "σ error") on each analysis which is estimated by considering a relative error of 1% on the external standard concentrations, and of 3% on the internal reference element (default parameters).

2.5 REE partition coefficients

The Nernst partition coefficient *D* is used to describe REE partitioning between carbonate and silicate liquids. This coefficient corresponds to a mass concentration ratio (in wt%) and is defined following the equation:

$$D_x^{CL/SL} = \frac{m_x^{CL}}{m_x^{SL}}. \quad (1)$$

with m_x^{CL} the mean concentration of the element *x* in the carbonate liquid (CL) and mx^{SL} the mean concentration in the silicate liquid (SL).

The standard deviation (i.e., the statistical uncertainty based on the number and the reproducibility of analysed samples) of each partition coefficient value, $\sigma\ (D_x^{CL/SL})$, has been calculated by error propagation from equation (2).

$$\sigma\left(D_x^{CL/SL}\right) = D_x^{CL/SL} * \sqrt{\left(\frac{\sigma_x^{CL}}{m_x^{CL}}\right)^2 + \left(\frac{\sigma_x^{SL}}{m_x^{SL}}\right)^2}. \quad (2)$$

with σ_x^{CL} and σ_x^{SL} the standard deviations of the mean concentrations m_x^{CL} and m_x^{SL}, respectively.

3. Results

3.1 Run product textures

The experiments were conducted at P-T conditions relevant to the evolution of alkaline magmas in the lithospheric mantle and the crust. At all P-T conditions, except at the lowest pressure (i.e., 0.2 GPa; Table 2 and Table A.1), the conditions of immiscibility were reached producing a carbonate liquid coexisting at equilibrium with an alkaline silica-undersaturated melt (Fig. 1). Among the 34-synthetised samples (Table 2), 23 of them present the characteristic of immiscibility between carbonate and silicate liquids and thus constitute the main focus of this study. In the other samples, only one melt (silicate or carbonate melt, see Table 2) coexisting or not with crystals occurs.

Silicate melts quenched into homogeneous and microlite-free glasses, while carbonate melts quenched into carbonate blebs with inter-crystallised Na-enriched and Ca-enriched bands (Fig. 1), which are

typical textures of unquenchable carbonate liquids (Brooker and Kjarsgaard, 2011; Martin et al., 2013). The attainment of equilibrium between the immiscible liquids at investigated P-T conditions is attested by the sharp geometry of the carbonate-silicate interfaces (Fig. 1), the homogeneity of the chemical composition of each liquid phase and the size of the carbonate liquid sections (i.e., up to 100µm). All these criteria exclude immiscibility by quench-related processes (Brooker and Kjarsgaard, 2011).

Bubble occurrence in most samples attests saturation in a fluid phase (Table 2). Clinopyroxene is the dominant crystalline phase, being present all along the crystallisation sequence, while, in strongly fractionated samples, other phases are present in significant proportions (i.e., titanite, spinel, calcite, nepheline, garnet, etc…; Fig. 1 and Table 2). The chemical features of the mineral phases are not discussed further, as this study focuses on liquid-liquid partitioning upon magmatic differentiation.

3.2 Composition of immiscible melts

The concentrations of major elements in the carbonate and silicate melts are presented in Table 3 (and Table A.1). Standard deviation on the compositions of each phase attests the homogeneity of the run products and equilibrium attainment.

The total alkali and silica contents of carbonate and silicate liquids at all experimental conditions are reported in a TAS diagram (Fig. 2a), classically used to discriminate magmatic rocks, and which shows the composition of the immiscible carbonate and silicate liquid couples at different experimental conditions. In response to variable degrees of crystallisation, the silicate liquid compositions vary from nephelinite to phonolite, with SiO_2 contents from 44.3 ± 0.7 to 55.6 ± 0.7 wt%, and Na_2O+K_2O contents from 14.7 ± 0.7 to 20.9 ± 0.5 wt% (on a volatile-free basis; Fig. 2a and Table 3). Silicate liquids with the lowest SiO_2 contents contain high CaO concentrations (Fig. 2b). The silicate liquid CaO contents decrease as crystals fractionation proceeds, in response to Ca-rich minerals formation (clinopyroxene and calcite; see Table 2). In all experimental run products, the silicate melts resulting from low to high degree of differentiation are peralkaline, i.e the alumina saturation index (ASI) defined as $Al_2O_3/(CaO+Na_2O+K_2O)$ on a molar basis (Shand, 1947) is lower than 1 and vary from 0.33 to 0.80 (Fig. 2c, Table 3). The peralkalinity of the silicate melts is also supported by the alkalinity index (AI) defined as Al_2O_3 - (Na_2O+K_2O) (molar basis; Shand, 1947) which is lower than 0 for all the samples (from -0.07 to -0.01; Table 3). The most differentiated silicate melts (lowest CaO contents) present the highest ASI, which indicates an evolution toward almost metaluminous compositions upon crystal-liquid fractionation. The alkali/alkaline-earth cation ratio $((Na_2O+K_2O)/(CaO+MgO)$; molar basis) of the silicate melts varies from low values for undifferentiated silicate melts, to high values for the most differentiated ones (Fig.2d). It is worth mentioning that both F and K doped samples have silicate melt compositions following the same trends (samples AK06_02 and AK08_03, Table 2 and Table 3), indicating that both elements do not affect this differentiation trend.

The coexisting carbonate liquids vary from 0.3 ± 0.2 to 9.2 ± 0.8 wt% SiO_2 (samples AK06_02 and AK02_04 respectively, Table 3), and from 6.8 ± 3.2 to 24.9 ± 3.3 wt% Na_2O+K_2O (T17_04 and AK06_02, Table 3; see Fig.2a). Carbonate liquids become richer in sodium and also poorer in calcium during the differentiation, as shown by the decrease of the CaO contents from 37.8 ± 1.6 to 20.9 ± 1.0 wt% (Table 3) along with an increase of the Na_2O contents from 5.1 ± 2.8 to 21.4 ± 1.9 wt% (Fig.3). The other major elements such as MgO and FeO do not present significant variation (see Table 3).

Both coexisting silicate and carbonate melts hence have compositions evolving during the differentiation, with peralkaline silicate liquids become alkali- and silica-richer while the coexisting carbonate liquids become highly alkaline and increasingly silica-poorer as temperature decreases and crystallisation proceeds.

3.3 REE partitioning between carbonate and silicate melts

REE concentrations in carbonate and silicate liquid phases were measured using LA-ICP-MS (Table 4 and Table A.2). Standard deviations on the compositions of each phase attests the homogeneity of the run products and equilibrium attainment (Table 4; the σ error is presented in Tables A.2 and A.3). Carbonate melt REE contents evolved from 150.5 ± 9.5 to 459.8 ± 30.2 µg/g (ppm) for the La as representative of other LREE, and from 5.9 ± 1.0 to 165.9 ± 52.9 µg/g for the Lu (see Table 4) as representative of other HREE. The silicate melt REE concentrations are lower, varying from 5.8 ± 0.5 to 100.4 ± 3.3 µg/g of La and from 1.9 ± 0.4 to 65.4 ± 2.8 µg/g of Lu (Table 4).

REE partition coefficients between carbonate and silicate liquids are presented in Table 5. For most of the experimental conditions, carbonate liquids are richer in REE than the coexisting silicate liquids (Fig. 4a, Table 4 and 5), but the partition coefficients vary greatly, from 1.6 ± 0.1 to 48.9 ± 4.4 for La, and from 0.48 ± 0.04 to 9.1 ± 0.7 for Lu. The variations are more important for light REE (LREE) than for heavy REE (HREE), since carbonate liquids are more enriched in LREE. The highest REE partition coefficients (Fig.4a) correspond to the most evolved carbonate and silicate melts, in other words to the most differentiated carbonate and silicate melts (Fig. 2 and 3). It is worth mentioning that no clear variation of $D_{REE}^{CL/SL}$ is observed with pressure and temperature, the highest partition coefficients corresponding to both the lowest and the highest P-T conditions (respectively 725°C – 0.4 GPa and 925°C – 1.5 GPa*;* Fig. 4a and Fig. A.1). Furthermore, no correlation has been observed for samples doped in graphite or water (see Table 2) and for K-rich sample (AK06_02, Tables 2 and 5).

One sample is doped in F compare to the other samples as mentioned in the 2.1 section (Table 2). We did not observe any relationships between the fluorine content and the REE partitioning, while the fluorine concentrations in carbonate melts varied from 0.8 to 14.9 wt% (Table 3 and 5, Fig. A.2). The highest La partition coefficients, 48.9 and 43.8, respectively correspond to carbonate melts containing 2.2 and 14.9 wt% F (Table 3 and 5, samples AK06_02 and AK08_03). Moreover, the F contents in the

silicate melts being often below the detection limit (Table 3), no correlation between F and La (as representative of other REE) partition coefficients could be observed.

We establish here a link between the REE concentrations of carbonatites and the differentiation of alkaline silicate magmas accounting for by the large variation of REE partition coefficients between carbonate and silicate melts. We plotted the La partition coefficient, $D_{La}^{CL/SL}$, as representative of other REE, as a function of the wt% CaO content in silicate melts (Fig. 4b), which is a good proxy of mineral fractionations during alkaline magma differentiation (Fig. 2b-d). In the experimental samples, the CaO content of the silicate melt decreases in response to the crystallisation of Ca-rich minerals during differentiation (section 3.2; Fig. 1 and Table 2). Fig. 4b clearly shows that La preferentially partitions in the carbonate liquid as crystal fractionation proceeds, establishing a direct link between carbonatite REE contents and differentiation of alkaline magmas.

Moreover, our data also show a very good correlation between both La and Ca partitioning (respectively $D_{La}^{CL/SL}$ and $D_{Ca}^{CL/SL}$; Fig. 4c). This correlation is also observed for other REE, though the correlation coefficient tends to decrease as the REE become heavier (Fig. A.3). This indicates that REE behave similarly to calcium, as expected given the similar ionic radii of REE^{3+} and Ca^{2+} (Shannon, 1976).

4. DISCUSSION

4.1 The differentiation effect on the REE contents of immiscible carbonatite.

REE partition coefficients between carbonate and silicate melts have been compared to previous investigation (grey dots, Fig. 4a). The same large variation observed in this study has also been noticed in literature data (Hamilton et al., 1989; Veksler et al., 1998; Veksler et al., 2012; Martin et al., 2013). Similarly, REE partition coefficients from other experimental studies, obtained in a vast range of P-T conditions (grey dots, Fig. 4a and Fig. A.1), essentially vary in response to changes in the melt composition. Such behaviour suggests that the large variation in REE partitioning shown in Fig. 4a is related to the change in the melt composition (Fig. 2a), being in turn due to crystal-liquid fractionation (Fig. 2b-d).

The correlation between both La and Ca partitioning (respectively $D_{La}^{CL/SL}$ and $D_{Ca}^{CL/SL}$, Fig. 4c) noticed in this study, and already highlighted in one previous study (Martin et al., 2013), is also observed in all the other experimental works (see grey dots in Fig.4c; Hamilton et al., 1989; Veksler et al., 2012). REE seem to behave similarly to calcium for all ranges of composition - i.e. K-rich (sample AK06_02 from this study; Martin et al., 2013), F-bearing (sample AK08_03 from this study; Veksler et al., 2012) and alkaline-rich (this study; Hamilton et al., 1989; Veksler et al., 2012) compositions - suggesting that the $D_{Ca}^{CL/SL}$ represents a powerful proxy for REE partitioning. In brief at the magmatic stage, Ca-rich carbonatites immiscible at equilibrium with Ca-poor alkaline silica-undersaturated magmas are the most enriched in REE, while carbonatites immiscible with Ca-rich alkaline magmas are the REE-poorest.

The crystal fractionation trend (i.e. $D_{La}^{CL/SL}$ vs the wt% CaO content in silicate melts) observed in our experiments is less clear for some of the previous experimental data (grey dots in Fig. 4b; Hamilton et al., 1989; Veksler et al., 2012). This scatter of the literature data indicates that the CaO content of the alkaline liquids is not the only parameter capturing the systematic behaviour of REE during immiscibility.

In order to optimise the use of this $D_{Ca}^{CL/SL}$ as a proxy for the $D_{REE}^{CL/SL}$, we propose below a series of parameterisations considering the molecular structure of the silicate melt.

4.2 Carbonatite REE composition modelling

A modelling framework is proposed to calculate REE composition of carbonate liquids from the compositions of the coexisting silicate liquids. This empirical modelling follows three successive steps, based on the results of the present study and the existing literature data: i) calculating the Ca partition coefficient ($D_{Ca}^{CL/SL}$) from the silicate liquid composition, ii) establishing the correlation between REE and Ca partition coefficients, iii) predicting REE concentrations of carbonatite, from the silicate liquid composition, by the combination of the previous steps.

4.2.1 $D_{Ca}^{CL/SL}$ modelling and melt structures

Based on an analyse of the correlation coefficients and considering the molecular configuration of REE in silicate melts, i.e. their ability to compete with other elements in the silicate melt structure (Ponader and Brown, 1989a; Mysen, 2004), the $D_{Ca}^{CL/SL}$ dependence on the silicate melt composition has been parameterised using three compositional terms: the silica content (SiO_2), the alumina saturation index noted ASI ($Al_2O_3/(CaO+Na_2O+K_2O)$) and the alkali/alkaline-earth cation ratio ($(Na_2O+K_2O)/(CaO+MgO)$) of the silicate melts. Each three parameters increase while the $D_{Ca}^{CL/SL}$ increases (Fig. 5a-c). These chemical parameters also changes as crystal fractionation proceeds (Fig. 2b-d): the liquid becomes silica-richer, evolves toward near-metaluminous composition ($Al_2O_3/(CaO+Na_2O+K_2O) \approx 1$) and Na rather than Ca increasingly dominate as charge compensator. At phonolitic stage, the three above-mentioned compositional terms show a maximum value (Fig. 2). Other compositional parameters have been tested (Mg #, Na_2O/K_2O, $(Na_2O+K_2O)/Al_2O_3$ and Y/Ho) but they did not show any clear correlation with the Ca partitioning and have thus been excluded from the parameterisation.

Noteworthy, introducing any pressure or temperature dependences did not yield better results. This chemical/structural formulation , however, account well for studies on the chemical environment of REE in silicate melts (Ellison and Hess, 1989; Ponader and Brown, 1989a), identifying the silica content, the degree of polymerisation and the role of Na as charge compensator as major parameters affecting the REE structural accommodation in silicate melts. Such changes in the molecular structure of coeval carbonate melts do not exist since these liquids remain a fully ionic and fully depolymerised structures

(McLennan and Taylor, 2012). Accordingly, in this parameterisation, the Ca and REE partitioning between silicate and carbonate melts are only ruled by the changes in the silicate melt compositions/structures. In the (primitive) peralkaline silicate liquid, Ca and REE contents can be relatively high, while these elements are not well accommodated in the silicate liquid close to metaluminous compositions; REE therefore tend to partition into the carbonate melt at equilibrium with composition close to the metaluminous join. Noteworthy, the CO_2 content in the silicate melt is not considered here but admittedly, it may play a role in REE behaviour.

The $D_{Ca}^{CL/SL}$ is formulated as a function of the three chemical/structural parameters as follows:

$$\ln\left(D_{Ca}^{CL/SL}\right) = a_0 + a_1 * SiO_2 + a_2 * \frac{Al_2O_3}{(CaO + Na_2O + K_2O)} + a_3 * \frac{(Na_2O + K_2O)}{(CaO + MgO)}. \quad (3)$$

Variables of equation (3) are defined on a molar basis (SiO_2, ASI and $(Na_2O+K_2O)/(CaO+MgO)$, in molar fractions).

The $D_{Ca}^{CL/SL}$ model is calibrated on a large experimental database (Freestone and Hamilton, 1980; Hamilton et al., 1989; Kjarsgaard et al., 1995; Jones et al., 1995; Brooker, 1998; Kjarsgaard, 1998; Veksler et al., 1998; Veksler et al., 2012; Martin et al., 2012; Martin et al., 2013; Massuyeau et al., 2015), which regroups 120 experimental data of immiscible carbonate and silicate liquids in natural-like systems, at pressure and temperature respectively ranging from 0.04 to 3.2 GPa and 700 to 1400 °C (Table 6). Synthetic systems (Kjarsgaard and Hamilton, 1988; Brooker and Hamilton, 1990; Lee and Wyllie, 1996; Brooker and Kjarsgaard, 2011; Keshav and Gudfinnsson, 2013; Novella et al., 2014) are excluded from this calibration because of their compositions being at odds with the alkaline magma systems. All the silicate melts from this experimental database (including data from this study) have composition evolving from strongly peralkaline to slightly metaluminous melts (ASI varies from 0.06 to 0.84; AI varies from -0.35 to 0.03; see Fig. 5b and Table 6). The calibration can thus be used for silicate melts of this range of composition, with the AI index between -0.35 and 0.05 and an ASI < 1. Moreover, as the lowest CaO contents in silicate melts used for the calibration is at 0.61 ± 0.03 wt% (this study, Table 3), the calculation can only be used for CaO higher than 0.50 wt%, in order to avoid extrapolation outside of the experimental database.

$D_{Ca}^{CL/SL}$ values from the experimental database are measured in volatile-bearing compositions. However, for practical reasons, the compositional variables are calculated on a volatile-free basis (i.e., composition casts oxides: SiO_2, TiO_2, Al_2O_3, FeO, MgO, CaO, Na_2O, K_2O): the reason being that the model will be used on natural alkaline silicate rocks, which have been degassed and whose volatile content is unknown.

A weighted least square regression has been used to parameterise this correlation (Mandel, 1964). This method is more accurate than a classical linear regression since it takes into account the uncertainty of

the measured $D_{Ca}^{CL/SL}$ (weight of 1/ σ ln ($D_{Ca}^{CL/SL}$)^2). This uncertainty has been calculated following the equation (2). The mean value of the measured relative uncertainty on both melts CaO contents is around 10 % (this study; Kjarsgaard, 1998; Martin et al., 2013; Massuyeau et al., 2015). To ensure that the regression method better takes into account the data with measured uncertainties, the uncertainty on the measured CaO contents of both the carbonate and silicate experimental liquids is defined as 20 % of the reported value when unspecified in the reference papers (i.e. Freestone and Hamilton, 1980; Hamilton et al., 1989; Kjarsgaard et al., 1995; Jones et al., 1995; Brooker, 1998; Veksler et al., 1998; Veksler et al., 2012). The regressed parameters a_0 to a_3 (eq. 3) are given in Table 7a.

The result of this regression is reported in the Fig. 6a. The measured $D_{Ca}^{CL/SL}$ are well reproduced, from the lowest values (close to 1) to the highest ones (around 40). The uncertainty on calculated $D_{Ca}^{CL/SL}$ is estimated by propagating errors (Meyer, 1975) obtained for the parameters a_0-a_3 with the following formulations:

$$\sigma^2_{ln(D_{Ca}^{CL/SL})} = \sigma^2_{a_0} + \sigma^2_{a_1} * (SiO_2)^2 + \sigma^2_{a_2} * \left(\frac{Al_2O_3}{CaO + Na_2O + K_2O}\right)^2 + \sigma^2_{a_3} * \left(\frac{Na_2O + K_2O}{CaO + MgO}\right)^2, \quad (4)$$

and

$$\sigma^2_{D_{Ca}^{CL/SL}} = D_{Ca}^{CL/SL^2} * \sigma^2_{ln(D_{Ca}^{CL/SL})}. \quad (5)$$

Equation (3) reproduces the experimental database within uncertainty, including the fluorine-rich ones (Fig. 6a) and enables the estimation of the $D_{Ca}^{CL/SL}$ solely from the silicate liquid composition. This allows us to predict the change in $D_{Ca}^{CL/SL}$ along the crystal fractionation occurring during alkaline melt differentiation.

4.2.2 $D_{REE}^{CL/SL} - D_{Ca}^{CL/SL}$ model.

La, Sm and Lu partition coefficients (respectively representing Light REE, intermediate REE and Heavy REE) are well correlated to the Ca partition coefficient (Fig. A.3). Martin et al. (2013) have noticed this correlation in their experimental results, and we validate this relationship in a much broader range of melt compositions and experimental conditions. A set of equation (Fig. A.3) linking $D_{REE}^{CL/SL}$ and $D_{Ca}^{CL/SL}$ has been calibrated against our data and the available literature data (Hamilton et al., 1989; Veksler et al., 2012; Martin et al., 2013). 53 experiments at pressure and temperature respectively ranging from 0.04 to 3.2 GPa and 725 to 1260°C have been used (Table 6). The $D_{REE}^{CL/SL}$ - $D_{Ca}^{CL/SL}$ regression (eq. 6) have also been parameterised by a weighted least square regression method (Mandel, 1964). The regressed parameters *a* to *b* are given in Table 7b for each REE.

From the calculated $D_{Ca}^{CL/SL}$, the $D_{REE}^{CL/SL}$ can be computed by applying the correlations identified for each REE (Fig 4c and Fig. A.3; Table 7b), following the equation:

$$D_{REE}^{CL/SL} = a * \left(D_{Ca}^{CL/SL}\right)^{b}. \quad (6)$$

The accuracy of the $D_{REE}^{CL/SL}$ - $D_{Ca}^{CL/SL}$ parameterisation can be appreciated in Fig. 6b. The mean uncertainty on the measured $D_{Ca}^{CL/SL}$ characterised in this study and Martin et al. (2013) is around 10%. For the studies where the uncertainty is not reported (Hamilton et al., 1989; Veksler et al., 2012), an error of 20% of the measured $D_{Ca}^{CL/SL}$ mean value has been applied. Given the average uncertainties reported on $D_{Ca}^{CL/SL}$, this procedure allows us to account for by the work of (Hamilton et al., 1989; Veksler et al., 2012), but this study and Martin et al. (2013) have then more weight and are more reliable in the parameterisation $D_{REE}^{CL/SL}$ - $D_{Ca}^{CL/SL}$ (Fig. 6b).

The uncertainty (Meyer, 1975) on the calculated $D_{REE}^{CL/SL}$ is calculated as follows:

$$\sigma^2_{D_{REE}^{CL/SL}} = a^2 * \left(\left(D_{Ca}^{CL/SL}\right)^b\right)^2 * \left[\left(\frac{b}{D_{Ca}^{CL/SL}}\right)^2 * \sigma^2_{D_{Ca}^{CL/SL}} + \left(\ln\left(D_{Ca}^{CL/SL}\right)\right)^2 * \sigma_b^2\right] + \left[\left(D_{Ca}^{CL/SL}\right)^b\right]^2 * \sigma_a^2. \quad (7)$$

with $\sigma\ (D_{Ca}^{CL/SL})$ the standard deviation on Ca partition coefficient and σ_a *and* σ_b the calculated uncertainty on the regressed parameter a and b.

For HREE, the correlations are less clear than for LREE and intermediate REE, as shown by $D_{Lu}^{CL/SL}$ (Fig. A.3). This may be due to the difference of ionic radii, since the radii of light and intermediate REE radii are similar to that of Ca, whereas HREE are smaller (Watson, 1976; Shannon, 1976). Likewise, the associated uncertainties are higher than for the other REE (Fig. 6b): this is probably due to the same reason and to the fact that the database (Hamilton et al., 1989; Veksler et al., 2012; Martin et al., 2013) is less complete for HREE than for LREE.

4.2.3 Calculation of carbonatite REE composition.

Equations (3) and (6) can be used to calculate the REE concentrations of the coexistent carbonate melt from the major elements and REE compositions of the silicate melt using the following equation:

$$m_{REE}^{CL} = m_{REE}^{SL} * D_{REE}^{CL/SL}. \quad (8)$$

with:

- m_{REE}^{SL} the natural mean concentration of REE in the silicate rocks,
- $D_{REE}^{CL/SL}$ the partition coefficient of REE calculated from the equation *(6)*.

The uncertainty on the calculated carbonate liquid REE concentrations is estimated by the following formulation:

$$\sigma^2_{m^{CL}_{REE-Y}} = \left(m^{SL}_{REE-Y}\right)^2 * \ \sigma^2_{D^{CL/SL}_{REE-Y}} + \left(D^{CL/SL}_{REE-Y}\right)^2 * \sigma^2_{m^{SL}_{REE-Y}}. \quad (9)$$

Using this methodology, we can predict the REE concentrations of any carbonatites in equilibrium with an alkaline silicate melt of known REE contents. Noteworthy, the two relationships (eq. 3 and 6) indicate, in agreement with literature data (Watson, 1976; Ponader and Brown, 1989a), that the depolymerised melts tend to better accommodate REE.

4.3 Predicting carbonatite REE magmatic enrichments

We propose two applications using these equations. The first one validates the method on a carbonatite and silica-undersaturated alkaline intrusive suite currently being explored for its REE content (Lofdal magmatic suite; Bodeving et al., 2017). The second one employs a large dataset of alkaline silicate rocks, in order to estimate the degree of enrichment of the carbonatites that could potentially be produced by immiscibility processes in the differentiation course of alkaline magmas.

4.3.1 Identifying coeval immiscible carbonate-silicate liquids

The first application concerns the Lofdal intrusive suite in Namibia that constitutes a textbook case where coeval carbonatites and silica-undersaturated magmas have been described (Bodeving et al., 2017). In fact, the carbonatite supposedly represents an immiscible liquid equilibrated with either phono-tephritic or phonolitic melts compositions that have been observed as volcanic dykes (Bodeving et al., 2017). The REE compositions of the carbonatite melt were calculated in equilibrium with the phono-tephritic and the phonolite melts of known REE content using eq. (3), (6) and (8). The calculated carbonatite magma formed at equilibrium with the phono-tephritic magma perfectly matches the REE composition of the Lofdal carbonatite (Fig.7). In contrast, carbonatites equilibrated with the phonolitic melt leads to calculated REE concentrations significantly higher than the Lofdal one: 1589 ppm of calculated La in the carbonatite, instead of 317 ppm in the natural carbonatite. This is due to the more fractionated nature of the phonolite, inducing a high calculated $D_{Ca}^{CL/SL}$ and high carbonatite REE contents. Thus, we conclude that the Lofdal carbonatite derives from the phono-tephrite rather than phonolite magmas; noteworthy, this methodology indicates that we can identify not only the composition of the coeval carbonate-silicate liquids but also at which magmatic stage the carbonate-silicate separation occurred in the crystallisation course of the alkaline magma. This validates our modelling and constitutes a promising tool for capturing the processes of formation of carbonatite melts.

4.3.2 Carbonatite REE enrichments across the differentiation course of alkaline magmas.

In the second application, we calculated the $D_{Ca}^{CL/SL}$ for natural alkaline silica-undersaturated magmatic rocks originating from two distinct geological settings (Fig. 8): the East-African Rift representing intracontinental rifting compositions, and the Canary and Cape Verde Islands representing hotspot settings on an oceanic lithosphere (data from GEOROC database and De Moor et al., 2013, Mattsson et

al., 2013 and Mana et al., 2015). In total 540 samples from GEOROC database (*http://georoc.mpch-mainz.gwdg.de/georoc/*) and 75 samples from additional publication (De Moor et al., 2013; Mattsson et al., 2013; Mana et al., 2015) were used for the East African Rift, including data from the Ol Doinyo Lengai volcano in Tanzania (De Moor et al., 2013), the most alkali-rich silicate rocks in Fig. 8a with Na_2O+K_2O > 15 wt% and 40-45 wt% of SiO_2 (arrow in Fig. 8a). For the Canary and the Cape Verde Islands, 686 and 312 samples were also selected (GEOROC database exclusively), respectively. For all settings, representative analyses of volcanic rocks belonging to the alkaline and hyper alkaline magmatic series were selected (melilite, basanite, foïdite, leucitite, nephelinite, tephrite, phono-tephrite, phonolite, and phono-trachyte), with respect to the limit of the modelling (i.e. AI, ASI and CaO contents of the silicate melts in the range of composition exposed in 4.2.1). We assume that immiscible carbonate melts can be produced at any stage along the differentiation course, though, it is unclear whether such immiscible processes can occur for primitive magma (Weidendorfer et al., 2016). The grey line in Fig. 8a separates the domain where immiscibility has been experimentally constrained from the domain where immiscibility may occur (Schmidt and Weidendorfer, 2018); in the latter domain, the current experimental dataset do not allow a firm statement yet (Fig. A.4). For both the East-African Rift and Island hotspot silicate compositions, the modelled $D_{Ca}^{CL/SL}$ are relatively low for melilitic to nephelinitic magmas and increase as both silica and total alkali contents increase across the alkaline magmatic series. The highest calculated Ca partition coefficients correspond to phonolitic and phono-trachytic compositions (Fig. 8a). Therefore, any carbonatites being immiscible with those silicate compositions must present a high REE-partition coefficients. Noteworthy, though the alkaline compositions shown in Fig. 8a may not all be subject to immiscibility, this study and many other experimental works leave no doubt on the fact that the phonolitic and phono-trachytic compositions, defining the REE enrichments optimum, can coexist with immiscible carbonate melts (Fig. A.4).

The REE compositions of alkaline silica-undersaturated rocks from the East African Rift and Island hotspots normalised to chondrite (McDonough and Sun, 1995) are shown in Fig. 9a and 10a respectively. From those alkaline magma REE compositions and the calculated $D_{Ca}^{CL/SL}$ (Fig. 8a), REE concentrations of the hypothetic immiscible carbonatites have been calculated. For the sake of simplicity, only calculated La and Lu abundances in carbonatites, respectively representing LREE and HREE, are plotted as a function of the CaO concentration in alkaline rocks (Fig. 8b). For all settings, the calculated REE concentrations in carbonatites increase as the CaO concentration decreases in the alkaline silicate magmatic rocks; the $D_{Ca}^{CL/SL}$ increases as indicated with the colour gradient in Fig. 8b. The carbonatites in equilibrium with fractionated alkaline magmas (lowest CaO concentrations) have then the highest REE concentrations and it can be noticed that the increase in REE content is asymptotic (Fig. 8b).

Finally, the chondrite-normalised REE profiles for carbonatites are shown in Fig. 9b for the East African Rift and in Fig.10b for Canary and Cape Verde Islands. In all cases, the REE-richest carbonatites corresponding to the highest $D_{Ca}^{CL/SL}$ (in red, Fig.9b and 10b) are calculated in equilibrium with

phonolitic/phono-trachytic magmas (Fig.8a). Their REE contents depend, in principle, on both the REE contents of the coeval silicate melts and the variations in the calculated $D_{Ca}^{CL/SL}$. However, the REE contents of the alkaline silicate rocks vary only by a factor of 10 (Fig. 9a and 10b), while the calculated REE concentration ranges for the equilibrium carbonatite melts vary by three order of magnitude (Fig. 9b and 10b), indicating a prime control by the immiscibility process. This process is, in turn, affected by the changes in the residual silicate liquid compositions upon differentiation.

Alkaline silicate rocks from the famous Ol Doinyo Lengai in Tanzania (grey arrow in Fig. 8a; data from De Moor et al., 2013), are not in the optimum of carbonatite REE enrichment, and are rather characterised by residual liquids evolving toward hyper-alkaline, silica depleted and Ca-rich compositions. Moreover, in Fig.11 which presents the AI index against the ASI of the alkaline silicate rocks used in this application from the three geological context, the optimum of REE enrichment correspond to composition slightly peralkaline to slightly metaluminous for the three locations ($D_{Ca}^{CL/SL}$ > 20; AI around -0.04 to 0.03; ASI around 0.70 to 1.0). The magmatic rocks from the Ol Doinyo Lengai volcano evolving toward strongly peralkaline compositions (AI from -0.26 to -0.05, Fig.11), are thus moving away from the optimum of carbonatite REE enrichments. This is consistent with the composition of natural natrocarbonatite from the Ol Doinyo Lengai volcano, which, at some magmatic stage, must coexist with these strongly peralkaline rocks, and are in fact less REE-rich compared to other carbonatites. The optimum of carbonatite REE enrichment is then rigorously restricted to phonolite / phono-trachyte with composition at the peralkaline-metaluminous boundary, as shown in Fig.11.

Calculated REE concentrations of carbonatites are compared to those of carbonatite REE deposits (grey field in Fig. 10). Only the most primary carbonatite compositions - the one which present the most primary characteristic (magmatic composition, texture and mineralogy) - have been chosen for the comparison (compositions selected in Verplanck et al., 2016). For the two geological settings, REE enrichments calculated for carbonatite melts in equilibrium with phonolitic magmas are similar to those observed in the REE-richest carbonatites: e.g., ∑REE > 30 000 ppm (Verplanck et al., 2016). Carbonatites formed by immiscibility processes with phonolitic magmas have concentrations comparable to those of carbonatite REE deposits, and are therefore candidates for the parental melts of some of these carbonatite-REE deposits. Such an assumption thus implies that in the course of the magmatic fractionation processes of alkaline melts where less fractionated silicate rocks dominated (e.g., tephrite, phono-tephrite), some pulses may occasionally yield REE-rich carbonatite sheets formed by immiscibility with a more evolved phonolitic melts. This may explain why in carbonatite REE deposits only a few dykes among hundreds are REE-enriched and thus highly enriched (Wall and Mariano, 1996; Castor, 2008; Yang et al., 2011; Néron et al., 2018).

Noteworthy, the crystallisation and fractionation of the carbonatite melt, and late- to post-magmatic fluid-mineral interactions constitute late stage processes affecting REE-distribution, as evidenced in

many carbonatites (Verplanck et al., 2016). The evolution of carbonatite composition in nature is often described as starting from a Ca-carbonatites, than Mg-carbonatites and finally Fe-carbonatites (Wall and Mariano, 1996), with decreasing temperature and increasing REE-contents. Fe-carbonatites are "late carbonatites" as described in Wall and Mariano (1996), and rather enriched in REE (Woolley and Kempe, 1989; Wall and Mariano, 1996; Verplanck et al., 2016). Ca-carbonatites may also present remarkable concentrations in REE (Yang et al., 2011; Verplanck et al., 2016). Nevertheless, late- to post- magmatic processes may obliterate the primary magmatic REE enrichments. Thus, fluids that are derived from magmatic exsolutions may remobilise the REE and transport them to form ore concentrations in the various carbonatite types (Ca-, Mg- and Fe- carbonatite). Those processes hence do not contradict this carbonatite REE enrichments modelling, as the parameterisation is based on the REE behaviour between carbonate and silicate melts at the magmatic stage, along the alkaline magma differentiation course. In the case of clearly identified late- to post- magmatic processes responsible of REE mineralisations in a natural carbonatite, as for the Lofdal Magmatic Suite in Namibia (4.3.1), this modelling can be apply to highlight the origin of the primary carbonate melt and to predict the timing of immiscibility between carbonatite and an associated alkaline rock, if a common origin is supposed.

Conversely to some carbonatites identified in the East African Rift (Wall and Mariano, 1996), the carbonatites occurring in the Canary and Cape Verde Islands are not particularly enriched in REE (Wallace, 1998; Hoernle et al., 2002; Mourão et al., 2010). However, the alkaline silicate melts of all settings broadly have the same REE concentration ranges (Fig. 9). This suggests that immiscibility did not occur in these oceanic settings at the phonolite/phono-trachytic stage, but at a rather more primitive stage (Wallace, 1998). One possible explanation for this is that at phonolitic stages, CO_2 degassing in the shallow plumbing system of these volcanoes may prevent immiscibility processes. Melt inclusions indeed show that CO_2 is a major constituent of primitive Canary Islands magmas (Wallace, 1998; Longpré et al., 2017), exceeding the weight percent level (Wiesmaier et al., 2011), whereas differentiated magmatic rocks do not present high CO_2 concentrations (Staudigel et al., 1986; Wiesmaier et al., 2011). For some reason, alkaline magmas from these oceanic settings must have lost their CO_2 content at early stage of differentiation preventing the formation of immiscible carbonatites at a phonolitic stage (Brooker, 1998). In the East-African rift, differentiated magma must still contain enough CO_2 to permit saturation in carbonatite melts from a silicate magma, which may be related to the dynamics of CO_2 flushing through the plumbing system (e.g., Fischer et al., 2009; De Moor et al., 2013). The fate of REE upon differentiation of alkaline magma must then not be only considered as controlled by fractionation processes since the (CO_2) degassing dynamics must also be taken into account.

5. CONCLUSION

This study provides a quantitative analyse of the fate of REE during the genesis of carbonatite melts by immiscibility with alkaline silicate magma. We show that the degree of fractionation of the alkaline magma when the carbonatite melt segregates plays a key role on REE-partitioning: primitive alkaline magma tends to retain REE while in fractionated phonolitic melts, carbonatites can efficiently concentrate the REE at levels of several wt-percent. This implies that the REE-content of carbonatite melts can be used to track the timing of their segregation from alkaline melts and to define both melt compositions at equilibrium. This also implies that magmatic processes producing highly REE-rich carbonatites are identified and that carbonatite produced at immiscibility with phonolitic melts present sufficient REE amounts to reach REE-deposits concentrations. Yet, carbonatite REE-deposits and most carbonatites worldwide are intrusive and do certainly not directly mirror the composition of carbonatite melts of interest in this study. Crystallization and late magmatic hydrothermal processes must be considered in order to fully address the range of REE contents of carbonatites.

Acknowledgements

This work, being part of Z. Nabyl PhD, was supported by the European Research Council (Grant no. 279790), the LABEX VOLTAIRE project (ANR-10-LABX-100-01) and the BRGM. We thank J-L. Devidal from the LMV laboratory (Laboratoire Magmas et Volcans, Clermont-Ferrand, France) for his support with LA-ICP-MS analysis and data treatment. We are grateful to Michael Marks, Charles Beard and an anonymous reviewer for their comments and thoughtful advices on this manuscript, and Ilya Veksler and another anonymous reviewer for constructive remarks on an earlier draft.

REFERENCES

Andújar J., Costa F. and Scaillet B. (2013) Storage conditions and eruptive dynamics of central versus flank eruptions in volcanic islands: The case of Tenerife (Canary Islands, Spain). *Journal of Volcanology and Geothermal Research* **260**, 62–79.

Aseri A. A., Linnen R. L., Che X. D., Thibault Y. and Holtz F. (2015) Effects of fluorine on the solubilities of Nb, Ta, Zr and Hf minerals in highly fluxed water-saturated haplogranitic melts. *Ore Geology Reviews* **64**, 736–746.

Bell K. and Simonetti A. (2010) Source of parental melts to carbonatites–critical isotopic constraints. *Miner Petrol* **98**, 77–89.

Blundy J. and Wood B. (2003) Partitioning of trace elements between crystals and melts. *Earth and Planetary Science Letters* **210**, 383–397.

Bodeving S., Williams-Jones A. E. and Swinden S. (2017) Carbonate–silicate melt immiscibility, REE mineralising fluids, and the evolution of the Lofdal Intrusive Suite, Namibia. *Lithos* **268–271**, 383–398.

Botcharnikov R. E., Linnen R. L., Wilke M., Holtz F., Jugo P. J. and Berndt J. (2011) High gold concentrations in sulphide-bearing magma under oxidizing conditions. *Nature Geoscience* **4**, 112–115.

Brooker R. A. (1998) The effect of CO_2 saturation on immiscibility between silicate and carbonate liquids: an experimental study. *J Petrology* **39**, 1905–1915.

Brooker R. A. and Hamilton D. L. (1990) Three-liquid immiscibility and the origin of carbonatites. *Nature* **346**, 459–462.

Brooker R. A. and Kjarsgaard B. A. (2011) Silicate–carbonate liquid immiscibility and phase relations in the system SiO2–Na_2O–Al_2O_3–CaO–CO_2 at 0.1–2.5 GPa with applications to carbonatite genesis. *J Petrology* **52**, 1281–1305.

Broom-Fendley S., Styles M. T., Appleton J. D., Gunn G. and Wall F. (2016) Evidence for dissolution-reprecipitation of apatite and preferential LREE mobility in carbonatite-derived late-stage hydrothermal processes. *American Mineralogist* **101**, 596–611.

Castor S. B. (2008) The Mountain Pass rare-earth carbonatite and associated ultrapotassic rocks, California. *The Canadian Mineralogist* **46**, 779–806.

Chakhmouradian A. R. and Wall F. (2012) Rare earth elements: minerals, mines, magnets (and more). *Elements* **8**, 333–340.

Chakhmouradian A. R. and Zaitsev A. N. (2012) Rare earth mineralization in igneous rocks: sources and processes. *Elements* **8**, 347–353.

Chebotarev D. A., Veksler I. V., Wohlgemuth-Ueberwasser C., Doroshkevich A. G. and Koch-Müller M. (2019) Experimental study of trace element distribution between calcite, fluorite and carbonatitic melt in the system $CaCO_3 + CaF_2 + Na_2CO_3 \pm Ca_3(PO_4)_2$ at 100 MPa. *Contrib Mineral Petrol* **174**, 4.

Dasgupta R., Hirschmann M. M. and Withers A. C. (2004) Deep global cycling of carbon constrained by the solidus of anhydrous, carbonated eclogite under upper mantle conditions. *Earth and Planetary Science Letters* **227**, 73–85.

Dasgupta R., Mallik A., Tsuno K., Withers A. C., Hirth G. and Hirschmann M. M. (2013) Carbon-dioxide-rich silicate melt in the Earth's upper mantle. *Nature* **493**, 211–215.

Davidson J., Turner S. and Plank T. (2013) Dy/Dy*: Variations arising from mantle sources and petrogenetic processes. *J Petrology* **54**, 525–537.

De Moor J. M., Fischer T. P., King P. L., Botcharnikov R. E., Hervig R. L., Hilton D. R., Barry P. H., Mangasini F. and Ramirez C. (2013) Volatile-rich silicate melts from Oldoinyo Lengai volcano (Tanzania): implications for carbonatite genesis and eruptive behavior. *Earth and Planetary Science Letters* **361**, 379–390.

Di Carlo I., Pichavant M., Rotolo S. G. and Scaillet B. (2006) Experimental crystallization of a high-K arc basalt: the Golden Pumice, Stromboli volcano (Italy). *J Petrology* **47**, 1317–1343.

Dostal J. (2016) Rare metal deposits associated with alkaline/peralkaline igneous rocks. In *Rare earth and critical elements in ore deposits* Reviews in Economic Geology. Verplanck PL & Hitzman MW, Littleton, CO, USA. pp. 33–54.

Doucelance R., Hammouda T., Moreira M. and Martins J. C. (2010) Geochemical constraints on depth of origin of oceanic carbonatites: The Cape Verde case. *Geochimica et Cosmochimica Acta* **74**, 7261–7282.

Duc-Tin Q. and Keppler H. (2015) Monazite and xenotime solubility in granitic melts and the origin of the lanthanide tetrad effect. *Contrib Mineral Petrol* **169**, 8.

Ellison A. J. G. and Hess P. C. (1989) Solution properties of rare earth elements in silicate melts: Inferences from immiscible liquids. *Geochimica et Cosmochimica Acta* **53**, 1965–1974.

Fischer T. P., Burnard P., Marty B., Hilton D. R., Füri E., Palhol F., Sharp Z. D. and Mangasini F. (2009) Upper-mantle volatile chemistry at Oldoinyo Lengai volcano and the origin of carbonatites. *Nature* **459**, 77–80.

Freestone I. C. and Hamilton D. L. (1980) The role of liquid immiscibility in the genesis of carbonatites — an experimental study. *Contr. Mineral. and Petrol.* **73**, 105–117.

Frost B. R. (1991) Introduction to oxygen fugacity and its petrologic importance. *Reviews in Mineralogy* **25**, 1–9.

Gaillard F., Scaillet B., Pichavant M. and Bény J.-M. (2001) The effect of water and fO_2 on the ferric–ferrous ratio of silicic melts. *Chemical Geology* **174**, 255–273.

Giebel R. J., Gauert C. D. K., Marks M. A. W., Costin G. and Markl G. (2017) Multi-stage formation of REE minerals in the Palabora Carbonatite Complex, South Africa. *American Mineralogist* **102**, 1218–1233.

Green D. H. and Wallace M. E. (1988) Mantle metasomatism by ephemeral carbonatite melts. *Nature* **336**, 459.

Hamilton D. L., Bedson P. and Esson J. (1989) The behaviour of trace elements in the evolution of carbonatites. In *Carbonatites, Genesis and Evolution* Bell K, London, UK. pp. 405–427.

Henderson P. (1984) *Rare Earth Element Geochemistry*., Elsevier, Amsterdam, NL.

Hoernle K., Tilton G., Le Bas M. J., Duggen S. and Garbe-Schönberg D. (2002) Geochemistry of oceanic carbonatites compared with continental carbonatites: mantle recycling of oceanic crustal carbonate. *Contrib Mineral Petrol* **142**, 520–542.

Jochum K. P., Weis U., Schwager B., Stoll B., Wilson S. A., Haug G. H., Andreae M. O. and Enzweiler J. (2016) Reference values following ISO guidelines for frequently requested rock reference materials. *Geostandards and Geoanalytical Research* **40**, 333–350.

Jones A. P., Genge M. and Carmody L. (2013) Carbonate melts and carbonatites. *Reviews in Mineralogy and Geochemistry* **75**, 289–322.

Jones J. H., Walker D., Pickett D. A., Murrell M. T. and Beattie P. (1995) Experimental investigations of the partitioning of Nb, Mo, Ba, Ce, Pb, Ra, Th, Pa, and U between immiscible carbonate and silicate liquids. *Geochimica et Cosmochimica Acta* **59**, 1307–1320.

Keppler H. (1993) Influence of fluorine on the enrichment of high field strength trace elements in granitic rocks. *Contr. Mineral. and Petrol.* **114**, 479–488.

Keshav S. and Gudfinnsson G. H. (2013) Silicate liquid-carbonatite liquid transition along the melting curve of model, vapor-saturated peridotite in the system CaO-MgO-Al_2O_3-SiO_2-CO_2 from 1.1 to 2 GPa. *Journal of Geophysical Research: Solid Earth* **118**, 3341–3353.

Kjarsgaard B. A. (1998) Phase relations of a carbonated high-CaO nephelinite at 0.2 and 0.5 GPa. *J Petrology* **39**, 2061–2075.

Kjarsgaard B. A. and Hamilton D. L. (1988) Liquid immiscibility and the origin of alkali-poor carbonatites. *Mineralogical Magazine* **52**, 43–55.

Kjarsgaard B. A. and Hamilton D. L. (1989) The genesis of carbonatites by immiscibility. In *Carbonatites, Genesis and Evolution* Bell K, London, UK. pp. 388–404.

Kjarsgaard B. A., Hamilton D. L. and Peterson T. D. (1995) Peralkaline nephelinite/carbonatite liquid immiscibility: comparison of phase compositions in experiments and natural lavas from Oldoinyo Lengai. In *Carbonatite Volcanism Ol Doinyo Lengai and the Petrogenesis of Natrocarbonatite*. IAVCEI Proceedings in Volcanology. Springer, Berlin, Heidelberg. pp. 163–190.

Le Bas M. J. (1981) Carbonatite magmas. *Mineralogical Magazine* **44**, 133–140.

Le Maitre R. W., Streckeisen A., Zanettin B., Bas M. J. L., Bonin B. and Bateman P. (2005) *Igneous rocks: a classification and glossary of terms: recommendations of the International Union of Geological Sciences Subcommission on the Systematics of Igneous Rocks*., Cambridge University Press.

Lee W. and Wyllie P. J. (1994) Experimental data bearing on liquid immiscibility, crystal fractionation, and the origin of calciocarbonatites and natrocarbonatites. *International Geology Review* **36**, 797–819.

Lee W.-J. and Wyllie P. J. (1996) Liquid immiscibility in the join NaAlSi3O8−CaCO3 to 2.5 GPa and the origin of calciocarbonatite magmas. *J Petrology* **37**, 1125–1152.

Linnen R. L., Samson I. M., Williams-Jones A. E. and Chakhmouradian A. R. (2014) Geochemistry of the rare-earth elements, Nb, Ta, Hf, and Zr deposits. In *Treatise on Geochemistry (Second Edition)* Holland HD, Turekian KK, Elsevier, Oxford. pp. 543–568.

Longpré M.-A., Stix J., Klügel A. and Shimizu N. (2017) Mantle to surface degassing of carbon- and sulphur-rich alkaline magma at El Hierro, Canary Islands. *Earth and Planetary Science Letters* **460**, 268–280.

Loubet M., Bernat M., Javoy M. and Allegre C. J. (1972) Rare earth contents in carbonatites. *Earth and Planetary Science Letters* **14**, 226–232.

Maimaiti M., Fabbrizio A., Carroll M. R., Ertel-Ingrisch W., Abudureheman A., Paris E. and Dingwell D. B. (2019) Experimental study of monazite solubility in haplogranitic melts: a new model for peraluminous and peralkaline melts. *European Journal of Mineralogy* **31**, 49–59.

Mana S., Furman T., Turrin B. D., Feigenson M. D. and Swisher C. C. (2015) Magmatic activity across the East African North Tanzanian Divergence Zone. *Journal of the Geological Society* **172**, 368–389.

Mandel J. (1964) *The statistical analysis of experimental data*., John Wiley & Sons, Inc, New York.

Martin L. H. J., Schmidt M. W., Mattsson H. B. and Guenther D. (2013) Element partitioning between immiscible carbonatite and silicate melts for dry and H2O-bearing systems at 1–3 GPa. *J Petrology* **54**, 2301–2338.

Martin L. H. J., Schmidt M. W., Mattsson H. B., Ulmer P., Hametner K. and Günther D. (2012) Element partitioning between immiscible carbonatite–kamafugite melts with application to the Italian ultrapotassic suite. *Chemical Geology* **320–321**, 96–112.

Massuyeau M., Gardés E., Morizet Y. and Gaillard F. (2015) A model for the activity of silica along the carbonatite–kimberlite–mellilitite–basanite melt compositional joint. *Chemical Geology* **418**, 206–216.

Mattsson H. B., Nandedkar R. H. and Ulmer P. (2013) Petrogenesis of the melilititic and nephelinitic rock suites in the Lake Natron–Engaruka monogenetic volcanic field, northern Tanzania. *Lithos* **179**, 175–192.

McDonough W. F. and Sun S. -s. (1995) The composition of the Earth. *Chemical Geology* **120**, 223–253.

McLennan S. M. and Taylor S. R. (2012) Geology, geochemistry, and natural abundances of the rare earth elements. In *The rare earth elements: fundamentals and applications* EIBC Books. Atwood DA, New York, NY, US. pp. 1–19.

Meyer S. L. (1975) *Data analysis for scientists and engineers*., John Wiley & Sons, Inc, New York, NY.

Migdisov A., Williams-Jones A. E., Brugger J. and Caporuscio F. A. (2016) Hydrothermal transport, deposition, and fractionation of the REE: Experimental data and thermodynamic calculations. *Chemical Geology* **439**, 13–42.

Mitchell R. H. (2005) Carbonatites and carbonatites and carbonatites. *The Canadian Mineralogist* **43**, 2049–2068.

Mourão C., Mata J., Doucelance R., Madeira J., Silveira A. B. da, Silva L. C. and Moreira M. (2010) Quaternary extrusive calciocarbonatite volcanism on Brava Island (Cape Verde): a nephelinite-carbonatite immiscibility product. *Journal of African Earth Sciences* **56**, 59–74.

Moussallam Y., Florian P., Corradini D., Morizet Y., Sator N., Vuilleumier R., Guillot B., Iacono-Marziano G., Schmidt B. C. and Gaillard F. (2016) The molecular structure of melts along the carbonatite–kimberlite–basalt compositional joint: CO_2 and polymerisation. *Earth and Planetary Science Letters* **434**, 129–140.

Mysen B. O. (2004) Element partitioning between minerals and melt, melt composition, and melt structure. *Chemical Geology* **213**, 1–16.

Mysen B. O. (1990) Relationships between silicate melt structure and petrologic processes. *Earth-Science Reviews* **27**, 281–365.

Naldrett A. J. (2010) Secular variation of magmatic sulfide deposits and their source magmas. *Economic Geology* **105**, 669–688.

Nelson D. R., Chivas A. R., Chappell B. W. and McCulloch M. T. (1988) Geochemical and isotopic systematics in carbonatites and implications for the evolution of ocean-island sources. *Geochimica et Cosmochimica Acta* **52**, 1–17.

Néron A., Bédard L. P. and Gaboury D. (2018) The Saint-Honoré Carbonatite REE Zone, Québec, Canada: combined magmatic and hydrothermal processes. *Minerals* **8**, 397.

Novella D., Keshav S., Gudfinnsson G. H. and Ghosh S. (2014) Melting phase relations of model carbonated peridotite from 2 to 3 GPa in the system CaO-MgO-Al_2O_3-SiO_2-CO_2 and further indication of possible unmixing between carbonatite and silicate liquids. *Journal of Geophysical Research: Solid Earth* **119**, 2780–2800.

Panina L. I. and Motorina I. V. (2008) Liquid immiscibility in deep-seated magmas and the generation of carbonatite melts. *Geochem. Int.* **46**, 448–464.

Pearce N. J. G., Perkins William T., Westgate John A., Gorton Michael P., Jackson Simon E., Neal Clive R. and Chenery Simon P. (1997) A compilation of new and published major and trace

element data for NIST SRM 610 and NIST SRM 612 glass reference materials. *Geostandards Newsletter* **21**, 115–144.

Ponader C. W. and Brown G. E. (1989a) Rare earth elements in silicate glassmelt systems: I. Effects of composition on the coordination environments of La, Gd, and Yb. *Geochimica et Cosmochimica Acta* **53**, 2893–2903.

Ponader C. W. and Brown G. E. (1989b) Rare earth elements in silicate glassmelt systems: II. Interactions of La, Gd, and Yb with halogens. *Geochimica et Cosmochimica Acta* **53**, 2905–2914.

Rocholl A. (1998) Major and trace element composition and homogeneity of microbeam reference material: basalt glass USGS BCR-2G. *Geostandards Newsletter* **22**, 33–45.

Rudnick R. L., McDonough W. F. and Chappell B. W. (1993) Carbonatite metasomatism in the northern Tanzanian mantle: petrographic and geochemical characteristics. *Earth and Planetary Science Letters* **114**, 463–475.

Schilling J.-G. and Winchester J. W. (1967) Rare-earth fractionation and magmatic processes. In *Mantles of the earth and terrestrial planets* Rundkorn SK, London, UK. pp. 267–283.

Schmidt M. W. and Weidendorfer D. (2018) Carbonatites in oceanic hotspots. *Geology* **46**, 435–438.

Shannon R. D. (1976) Revised effective ionic radii and systematic studies of interatomic distances in halides and chalcogenides. *Acta Crystallogr* **32**, 751–767.

Smith M. P., Moore K., Kavecsánszki D., Finch A. A., Kynicky J. and Wall F. (2016) From mantle to critical zone: a review of large and giant sized deposits of the rare earth elements. *Geoscience Frontiers* **7**, 315–334.

Song W., Xu C., Veksler I. V. and Kynicky J. (2016) Experimental study of REE, Ba, Sr, Mo and W partitioning between carbonatitic melt and aqueous fluid with implications for rare metal mineralization. *Contrib Mineral Petrol* **171**, 1.

Staudigel H., Feraud G. and Giannerini G. (1986) The history of intrusive activity on the island of La Palma (Canary Islands). *Journal of Volcanology and Geothermal Research* **27**, 299–322.

Tappe S., Romer R. L., Stracke A., Steenfelt A., Smart K. A., Muehlenbachs K. and Torsvik T. H. (2017) Sources and mobility of carbonate melts beneath cratons, with implications for deep carbon cycling, metasomatism and rift initiation. *Earth and Planetary Science Letters* **466**, 152–167.

Van Achterbergh E., Ryan C. and Griffin W. (2001) GLITTER user's manual: on-line interactive data reduction for the LA-ICP-MS microprobe. Version 4.

Veksler I. V., Dorfman A. M., Dulski P., Kamenetsky V. S., Danyushevsky L. V., Jeffries T. and Dingwell D. B. (2012) Partitioning of elements between silicate melt and immiscible fluoride, chloride, carbonate, phosphate and sulfate melts, with implications to the origin of natrocarbonatite. *Geochimica et Cosmochimica Acta* **79**, 20–40.

Veksler I. V., Dorfman A. M., Kamenetsky M., Dulski P. and Dingwell D. B. (2005) Partitioning of lanthanides and Y between immiscible silicate and fluoride melts, fluorite and cryolite and the origin of the lanthanide tetrad effect in igneous rocks. *Geochimica et Cosmochimica Acta* **69**, 2847–2860.

Veksler I. V., Petibon C., Jenner G. A., Dorfman A. M. and Dingwell D. B. (1998) Trace element partitioning in immiscible silicate–carbonate liquid systems: an initial experimental study using a centrifuge autoclave. *J Petrology* **39**, 2095–2104.

Verplanck P. L., Mariano A. N. and Jr A. M. (2016) Rare earth element ore geology of carbonatites. **18**, 5–32.

Wall F. (2014) Rare earth elements. In *Critical Metals Handbook* John Wiley & Sons, Ltd. pp. 312–339.

Wall F. and Mariano A. (1996) Rare earth minerals in carbonatites: a discussion centred on the Kangankunde Carbonatite, Malawi. In *Rare Earth Minerals, Chemistry, Origin and Ore Deposits, Mineralogical Society Series* Jones AP, Wall F, & Williams CT, London, UK. pp. 193–226.

Wallace M. E. and Green D. H. (1988) An experimental determination of primary carbonatite magma composition. *Nature* **335**, 343–346.

Wallace P. (1998) Pre-eruptive H2O and CO2 contents of mafic magmas from the submarine to emergent shield stages of Gran Canaria. In *Proceedings of the Ocean Drilling Program. Scientific Results, Gran Canaria and Madeira Abyssal Plain, Sites 950-956* Weaver PPE, Schmincke H-U, Firth JV, & Duffield W, College station, TX. pp. 411–420.

Watson E. B. (1976) Two-liquid partition coefficients: experimental data and geochemical implications. *Contr. Mineral. and Petrol.* **56**, 119–134.

Watson E. B. (1979) Zircon saturation in felsic liquids: experimental results and applications to trace element geochemistry. *Contr. Mineral. and Petrol.* **70**, 407–419.

Weidendorfer D., Schmidt M. W. and Mattsson H. B. (2017) A common origin of carbonatite magmas. *Geology* **45**, 507–510.

Weidendorfer D., Schmidt M. W. and Mattsson H. B. (2016) Fractional crystallization of Si-undersaturated alkaline magmas leading to unmixing of carbonatites on Brava Island (Cape Verde) and a general model of carbonatite genesis in alkaline magma suites. *Contrib Mineral Petrol* **171**, 43.

Wiesmaier S., Deegan F. M., Troll V. R., Carracedo J. C., Chadwick J. P. and Chew D. M. (2011) Magma mixing in the 1100 AD Montaña Reventada composite lava flow, Tenerife, Canary Islands: interaction between rift zone and central volcano plumbing systems. *Contrib Mineral Petrol* **162**, 651–669.

Wilkinson J. J. (2013) Triggers for the formation of porphyry ore deposits in magmatic arcs. *Nature Geoscience* **6**, 917–925.

Woolley A. R. and Kempe D. R. C. (1989) Carbonatites: nomenclature, average chemical compositions, and element distribution. In *Carbonatites, genesis and evolution* Bell K, London, UK. pp. 1–14.

Woolley A. R. and Kjarsgaard B. A. (2008) Paragenetic types of carbonatite as indicated by the diversity and relative abundances of associated silicate rocks: evidence from a global database. *The Canadian Mineralogist* **46**, 741–752.

Yang K.-F., Fan H.-R., Santosh M., Hu F.-F. and Wang K.-Y. (2011) Mesoproterozoic carbonatitic magmatism in the Bayan Obo deposit, Inner Mongolia, North China: constraints for the mechanism of super accumulation of rare earth elements. *Ore Geology Reviews* **40**, 122–131.

Yang L. and Van Hinsberg V. J. (2019) Liquid immiscibility in the CaF2-granite system and trace element partitioning between the immiscible liquids. *Chemical Geology* **511**, 28–41.

Declaration of interests

☒ The authors declare that they have no known competing financial interests or personal relationships that could have appeared to influence the work reported in this paper.

☐The authors declare the following financial interests/personal relationships which may be considered as potential competing interests:

Table 1. Chemical composition of the synthetised starting materials, composed of synthetic nephelinite powder and synthetic calcite (in a ratio 90:10). Mix 9 is K-richer (Mix 8 and additional K_2CO_3 in a ratio of 95:5 respectively) and Mix 10 is F and Ca-richer (Mix 8 and additional CaF_2 in a ratio of 97:3 respectively). Major elements (weight %) and trace elements (µg/g, i.e. ppm) of Mix8 and Mix 9 were analysed by ICP-MS analysis on powders (ALS Global). F, Cl and all the Mix 10 have not been analysed: concentrations are calculated on a normalised basis (*).

Table 2. Experimental conditions and run products. P: total pressure; T: temperature; H_2: partial pressure of hydrogen; SL: silicate liquid; CL: carbonate liquid; CPx: clinopyroxene (diopside-hedenbergite-aegirine solution); Cc: calcite; Ttn: titanite; Fe-Spl: iron-spinel (magnetite-titanomagnetite solid solution); Al-Spl: alumino-spinel; Ilm: ilmenite; Nph: nepheline; Afs: alkali feldspar; Prv: perovskite; Ap: apatite; Gnt: garnet (andradite); Mll: melilite; Phl: phlogopite; V: vapour phase; *: estimated from mass balance.

Table 3. Major element compositions of experimental silicate and carbonate liquids (weight %) analysed by EMPA; SL: silicate liquid; CL: carbonate liquid; Bdl: below detection limit; s.d.: standard deviation, statistical uncertainty calculated on the mean value. The AI, ASI and Fe# are in molar fraction.

Table 4. Trace elements concentrations of experimental silicate and carbonate liquids (µg/g, i.e. ppm) measured by LA-ICP-MS. SL: silicate liquid; CL: carbonate liquid; bdl: below detection limit; s.d.: standard deviation, statistical uncertainty calculated on the mean value; *: sample analysed by the Thermo Element XR ICP-MS; #: sample analysed by the Agilent 7500 CS ICP-MS.

Table 5. Trace elements and calcium partition coefficients between silicate and carbonate liquids. s.d.: standard deviation, calculated statistical uncertainty.

Table 6. Experimental database of immiscible carbonate and silicate melts used for the modelling of carbonatite REE compositions. All studies were used for the $D_{Ca}^{CL/SL}$ calculation. Only the studies with * were used for the $D_{REE}^{CL/SL}$-$D_{Ca}^{CL/SL}$ modelling and carbonatite REE composition calculation. N: number of experiments; P: pressure; T: temperature; SL: silicate liquid; CL: carbonate liquid; SiO_2 and CaO contents of the silicate melts or in wt %. AI (alkalinity index) and ASI (alumina saturation index) of the silicate melts are in molar fractions.

Table 7. Calculated coefficients and associated errors used for the modelling. a. Coefficients calculated for the $D_{Ca}^{CL/SL}$ parameterisation from the silicate liquid composition. b. Coefficients calculated from the $D_{REE}^{CL/SL}$ calculation (weighted least square regression for both calculations); SL: silicate liquid; CL: carbonate liquid.

	Mix 8	Mix 9	Mix 10*
Major elements in weight %			
SiO_2	35.39	33.31	34.80
TiO_2	1.70	1.61	1.78
Al_2O_3	11.34	10.88	11.07
Fe_2O_3	9.26	8.84	8.98
MnO	0.26	0.25	0.25
MgO	2.05	1.93	1.66
CaO	15.67	14.79	17.74
Na_2O	7.22	6.86	7.38
K_2O	2.85	5.75	2.84
P_2O_5	0.31	0.28	0.29
SrO	0.46	0.43	0.44
BaO	0.26	0.24	0.25
F	0.14 *	0.13 *	1.31
Cl	0.13 *	0.13 *	0.13
LOI	12.96	14.55	11.07
Total	100	100	100
Trace elements in µg/g (ppm)			
Ba	2300	2110	2353
Sr	4080	3750	3820
Nb	276	263	261
La	86.6	83.1	71
Ce	93.2	88.5	71
Pr	60	57.1	71
Nd	63.2	59.8	71
Sm	56.4	55.1	71
Eu	61.2	56	71
Gd	59.4	63.7	71
Tb	52	51.9	71
Dy	58.5	58.7	71
Ho	56	54.9	71
Er	57	55.3	71
Yb	58.7	57.4	71
Lu	53.8	52.1	71
Y	70.1	65.7	71

Table 1. Chemical composition of the synthetised starting materials, composed of synthetic nephelinite powder and synthetic calcite (in a ratio 90:10). Mix 9 is K-richer (Mix 8 and additional K_2CO_3 in a ratio of 95:5 respectively) and Mix 10 is F and Ca-richer (Mix 8 and additional CaF_2 in a ratio of 97:3 respectively). Major elements (weight %) and trace elements (µg/g) of Mix8 and Mix 9 were analysed by ICP-MS analysis on powders (ALS Global). F, Cl and all the Mix 10 have not been analysed: concentrations are calculated on a normalised basis (*).

Experiment	Starting material	P (Gpa)	T (°C)	H_2 (Mpa)	Duration (h)	Capsule material	Added water (wt %)	Added graphite (wt %)	Observed phases
T14_01	Mix 8	0.8	975	-	116	$Au_{80}Pd_{20}$	-	-	SL + CL + CPx + Fe-Spl + Gnt + V
T14_02	Mix 8	0.8	975	-	116	$Au_{80}Pd_{20}$	0.2	-	SL + CL + CPx + Fe-Spl + Gnt + V
T16_01	Mix 8	0.8	950	-	118.5	$Au_{80}Pd_{20}$	-	-	SL + CL + CPx + Ttn* + Gnt* + V
T16_02	Mix 8	0.8	950	-	118.5	$Au_{80}Pd_{20}$	-	1	SL + CL + CPx + Nph + Fe-Spl*
T16_03	Mix 8	0.8	950	-	118.5	$Au_{80}Pd_{20}$	4.5	-	SL + CPx* + Fe-Spl + V
T16_04	Mix 8	0.8	950	-	118.5	$Au_{80}Pd_{20}$	5.4	1	V + SL
T18_01	Mix 8	1.5	925	-	118.5	$Au_{80}Pd_{20}$	-	-	SL + CL + CPx + Cc + Fe-Spl + Afs + V
T18_02	Mix 8	1.5	925	-	118.5	$Au_{80}Pd_{20}$	-	1	CL + CPx + Al-Spl + Ilm + Nph + Afs + V
T18_03	Mix 8	1.5	925	-	118.5	$Au_{80}Pd_{20}$	2.1	-	SL + CL + CPx + Cc + Fe-Spl
T18_04	Mix 8	1.5	925	-	118.5	$Au_{80}Pd_{20}$	1	1	SL + CL + CPx + Cc + Fe-Spl
T17_01	Mix 8	0.8	925	-	119	$Au_{80}Pd_{20}$	-	-	SL + CL + CPx + Ttn + Fe-Spl + Gnt + V
T17_02	Mix 8	0.8	925	-	119	$Au_{80}Pd_{20}$	-	1	SL + CL + CPx + Ttn + Nph + Afs + Cc* + Fe-Spl* + Ap* + V
T17_03	Mix 8	0.8	925	-	119	$Au_{80}Pd_{20}$	4	-	SL + CPx* + Fe-Spl + V
T17_04	Mix 8	0.8	925	-	119	$Au_{80}Pd_{20}$	3	1	SL + CL + CPx + Fe-Spl + V
AK02_01	Mix 8	0.4	925	0.5	118	Au	-	-	SL + CL + CPx + Cc +Ttn + Fe-Spl* + V
AK02_02	Mix 8	0.4	925	0.5	118	Au	-	1	SL + CL + CPx + Cc + Ttn + Al-Spl + Nph + Prv + V
AK02_03	Mix 8	0.4	925	0.5	118	Au	1.6	-	SL + Cpx + Fe-Spl* + V
AK02_04	Mix 8	0.4	925	0.5	118	Au	1	1	SL + CL + CPx +Ttn + Fe-Spl* + V
AK01_01	Mix 8	0.2	925	0.5	122	Au	-	-	SL + CPx + Al-Spl + Nph + Prv + Ap + Mll + V
AK01_02	Mix 8	0.2	925	0.5	122	Au	-	1	SL + Al-Spl + Nph + Prv + Ap + Mll + V
AK01_03	Mix 8	0.2	925	0.5	122	Au	1.3	-	SL + Cpx + Prv + Gnt + Mll + V
AK01_04	Mix 8	0.2	925	0.5	122	Au	2.7	1	SL + Cpx + Prv + Mll + V
T19_01	Mix 8	0.8	850	-	120.5	$Au_{80}Pd_{20}$	-	-	SL + CL + CPx + Cc + Ttn + Fe-Spl + Nph + Afs + V
T19_02	Mix 8	0.8	850	-	120.5	$Au_{80}Pd_{20}$	-	1	CL + CPx + Cc + Ttn + Fe-Spl + Ilm + Nph + Afs + V
T19_03	Mix 8	0.8	850	-	120.5	$Au_{80}Pd_{20}$	3	-	SL + CL + CPx + Cc + Ttn + Fe-Spl + Ap + V
T19_04	Mix 8	0.8	850	-	120.5	$Au_{80}Pd_{20}$	3	1	SL + CL + CPx + Cc + Ttn + Fe-Spl + Nph + V
AK05_01	Mix 8	0.4	825	0.1	63	Au	-	-	SL + CL + CPx + Cc + Ttn + Fe-Spl + Nph + Ap + V
AK05_02	Mix 8	0.4	825	0.1	63	Au	2	-	SL + CL + CPx + Cc + Ttn + Fe-Spl + Ap + V
AK05_03	Mix 8	0.4	825	0.1	63	Au	4	-	SL + CL + CPx + Cc + Ttn + Fe-Spl + Ap + Gnt + V
AK05_04	Mix 8	0.4	825	0.1	63	Au	2	1	CL + CPx + Cc + Ttn + Fe-Spl + Nph + Afs + V
AK05_05	Mix 8	0.4	825	0.1	63	Au	10	-	SL + CL + CPx + Cc + Fe-Spl + Ap + Gnt + V
AK06_01	Mix 8	0.4	725	0.1	450	Au	5	-	SL + CL + CPx + Cc + Ttn + Fe-Spl + Ap + Gnt + Phl + V
AK06_02	Mix 9	0.4	725	0.1	450	Au	5	-	SL + CL + CPx + Cc + Ttn + Fe-Spl + Ap + Gnt + Phl + V
AK08_03	Mix 10	0.4	725	0.1	140.5	Au	5	-	SL + CL + CPx + Cc + Ttn + Fe-Spl + V

Table 2. Experimental conditions and run products. P: total pressure; T: temperature; H_2: partial pressure of hydrogen; SL: silicate liquid; CL: carbonate liquid; CPx: clinopyroxene (diopside-hedenbergite-aegirine solution); Cc: calcite; Ttn: titanite; Fe-Spl: iron-spinel (magnetite-titanomagnetite solid solution); Al-Spl: alumino-spinel; Ilm: ilmenite; Nph: nepheline; Afs: alkali feldspar; Prv: perovskite; Ap: apatite; Gnt: garnet (andradite); Mll: melilite; Phl: phlogopite; V: vapour phase; *: estimated from mass balance.

Experiment	T14_01		T14_02		T16_01		T16_02		T18_01		T18_03		T18_04		T17_01		T17_02		T17_04		AK02_01		AK02_02	
P (GPa)	0.8		0.8		0.8		0.8		1.5		1.5		1.5		0.8		0.8		0.8		0.4		0.4	
T (°C)	975		975		950		950		925		925		925		925		925		925		925		925	
SL																								
Analysis	11		10		5		5		5		6		9		5		9		17		14		5	
		s.d.		s.d.		s.d.		s.d.		s.d.		s.d.	s.d.	s.d.		s.d.		s.d.		s.d.		s.d.		s.d.
SiO_2	47.24	0.71	48.14	0.59	39.90	0.59	44.31	1.82	52.13	1.24	47.01	0.81	49.99	0.87	46.82	1.15	48.20	1.58	38.87	0.60	43.16	0.80	48.21	1.07
TiO_2	0.95	0.12	0.94	0.12	1.84	0.16	2.01	0.11	0.87	0.08	1.07	0.14	0.94	0.12	1.30	0.19	1.34	0.26	1.70	0.16	1.14	0.09	0.86	0.10
Al_2O_3	17.04	0.37	19.26	0.40	13.45	0.14	14.55	1.32	20.40	0.41	16.37	0.48	17.74	0.33	17.46	0.19	18.33	0.52	13.18	0.19	16.05	0.32	18.19	0.54
FeO	4.55	0.23	3.94	0.39	8.07	0.24	5.33	0.59	3.42	0.16	4.71	0.46	4.40	0.24	5.74	0.28	5.04	0.70	7.43	0.33	6.33	0.42	4.13	0.39
MnO	bdl	-	bdl	-	0.33	0.04	0.33	0.00	bdl	-	bdl	-	bdl	-	bdl	-	bdl	-	bdl	-	bdl	-	bdl	-
MgO	0.93	0.08	0.57	0.03	1.28	0.05	0.80	0.09	0.30	0.02	0.70	0.02	0.61	0.02	0.66	0.09	0.44	0.05	1.25	0.04	0.83	0.00	0.52	0.02
CaO	7.05	0.35	4.96	0.41	10.76	0.26	11.31	1.22	1.67	0.03	4.28	0.11	2.85	0.11	5.23	0.59	4.09	0.57	11.49	0.33	8.82	0.17	4.94	0.32
Na_2O	8.95	0.40	9.51	0.45	9.86	0.12	10.05	0.53	9.54	0.60	8.53	1.12	9.23	0.63	10.16	0.80	11.40	0.39	9.20	0.21	8.90	0.40	10.28	0.50
K_2O	4.56	0.22	5.15	0.14	3.63	0.13	4.10	0.40	6.25	0.54	4.64	0.12	4.87	0.10	5.10	0.23	5.57	0.20	3.74	0.16	4.39	0.22	4.91	0.10
P_2O5	bdl	-	bdl	-	bdl	-	bdl	-	bdl	-	bdl	-	bdl	-	bdl	-	bdl	-	bdl	-	bdl	-	bdl	-
BaO	bdl	-	bdl	-	bdl	-	bdl	-	bdl	-	bdl	-	bdl	-	bdl	-	bdl	-	bdl	-	bdl	-	bdl	-
SrO	bdl	-	bdl	-	bdl	-	bdl	-	bdl	-	bdl	-	bdl	-	bdl	-	bdl	-	bdl	-	bdl	-	bdl	-
F	0.62	0.14	bdl	-	bdl	-	bdl	-	bdl	-	0.59	0.07	bdl	-	0.55	0.20	bdl	-	0.73	0.24	bdl	-	1.03	0.12
Cl	0.14	0.03	0.12	0.02	0.16	0.02	0.16	0.02	0.12	0.02	0.14	0.02	0.15	0.01	0.11	0.04	0.12	0.02	0.16	0.02	0.19	0.03	0.14	0.02
Total	92.03	-	92.59	-	89.27	-	92.95	-	94.72	-	88.04	-	90.78	-	93.03	-	94.53	-	87.74	-	89.81	-	93.20	-
Na_2O+K_2O	13.51	0.62	14.66	0.59	13.49	0.24	14.15	0.93	15.79	1.14	13.17	1.24	14.10	0.73	15.26	1.03	16.97	0.59	12.94	0.37	13.29	0.63	15.19	0.60
AI [$Al_2O-(Na_2O+K_2O)$]	-0.02		-0.01		-0.05		-0.04		-0.01		-0.02		-0.02		-0.03		-0.05		-0.04		-0.02		-0.03	
ASI [$Al_2O_3/(CaO+Na_2O+K_2O)$]	0.52		0.64		0.34		0.35		0.80		0.61		0.69		0.55		0.57		0.33		0.45		0.58	
Fe # [FeO/(FeO+MgO)]	0.73		0.80		0.78		0.79		0.86		0.79		0.80		0.85		0.87		0.77		0.81		0.82	
CL																								
Analysis	6		8		4		5		4		4		6		4		6		7		12		7	
		s.d.		s.d.		s.d.		s.d.		s.d.		s.d.		s.d.		s.d.		s.d.		s.d.		s.d.		s.d.
SiO_2	3.61	1.23	1.15	0.54	4.83	0.66	3.51	0.97	0.44	0.12	3.20	1.59	1.95	0.70	2.56	0.76	1.58	0.33	7.76	2.82	6.98	0.82	3.46	0.25
TiO_2	0.32	0.18	bdl	-	0.54	0.06	0.51	0.10	bdl	-	bdl	-	bdl	-	0.40	0.12	0.42	0.11	0.97	0.24	0.54	0.07	bdl	-
Al_2O_3	0.47	0.14	bdl	-	0.55	0.12	0.19	0.09	0.10	0.01	0.94	0.54	0.40	0.20	0.27	0.07	0.11	0.05	1.59	0.64	0.82	0.19	0.24	0.03
FeO	1.09	0.42	0.96	0.20	2.93	0.48	2.28	0.30	6.03	0.29	5.02	2.15	5.91	0.51	3.47	0.82	3.17	0.71	3.84	1.34	4.76	0.61	3.39	0.26
MnO	bdl	0.08	bdl	-	0.34	0.03	0.24	0.05	0.76	0.13	0.88	0.32	0.62	0.09	0.46	0.11	0.44	0.07	0.31	0.05	bdl	-	0.45	0.06
MgO	1.79	0.52	1.35	0.21	1.86	0.44	0.94	0.29	2.49	0.21	2.42	0.63	3.08	0.17	1.75	0.40	0.94	0.21	1.70	0.79	1.38	0.16	0.99	0.09
CaO	35.80	1.67	37.75	1.58	35.17	1.18	37.19	1.64	27.96	0.26	26.14	4.59	29.44	1.50	35.38	1.47	33.03	1.59	35.87	3.76	34.43	1.93	36.44	1.71
Na_2O	8.80	1.68	9.77	1.91	8.78	2.27	9.72	2.80	14.16	0.78	10.02	4.56	10.00	1.80	10.23	2.39	14.55	1.66	5.09	2.77	7.81	1.89	9.16	2.22
K_2O	1.66	0.27	1.78	0.26	1.72	0.20	2.16	0.34	1.91	0.22	1.24	0.65	1.17	0.31	1.61	0.36	2.49	0.18	1.74	0.42	2.04	0.31	2.06	0.35
P_2O5	0.89	0.36	1.64	0.44	1.04	0.70	1.64	0.37	1.66	0.45	4.85	4.31	1.72	0.35	1.83	0.37	1.22	0.37	1.48	1.18	2.02	0.38	1.72	0.37
BaO	0.86	0.11	0.98	0.10	0.99	0.33	0.96	0.20	0.98	0.19	1.05	0.31	1.24	0.14	1.07	0.31	0.81	0.16	0.70	0.14	0.72	0.05	0.82	0.11
SrO	1.97	0.20	1.92	0.10	1.47	0.06	1.65	0.17	1.24	0.26	1.07	0.24	1.30	0.19	1.87	0.31	1.35	0.26	1.31	0.17	1.41	0.16	1.68	0.18
F	2.45	0.69	2.20	0.79	3.49	0.81	4.04	2.87	2.17	0.46	2.58	1.14	2.12	0.29	5.36	3.05	2.62	1.45	2.21	0.93	1.40	0.31	2.28	1.14
Cl	0.22	0.14	0.44	0.17	0.36	0.18	0.20	0.09	0.61	0.33	0.27	0.09	0.27	0.07	0.29	0.07	0.29	0.08	0.11	0.04	0.40	0.18	0.26	0.04
Total	59.94	-	59.95	-	64.06	-	65.23	-	60.51	-	58.61	-	59.22	-	66.53	-	63.01	-	64.66	-	64.71	-	62.94	-
Na_2O+K_2O	10.46	1.95	11.55	2.17	10.50	2.47	11.88	3.14	16.08	1.00	11.26	6.17	11.16	2.11	11.84	2.75	17.04	1.84	6.83	3.20	9.85	2.20	11.22	2.57

Table 3. Major element compositions of experimental silicate and carbonate liquids (weight %) analysed by EMPA; SL: silicate liquid; CL: carbonate liquid; Bdl: below detection limit; s.d.: standard deviation, statistical uncertainty calculated on the mean value. The AI, ASI and Fe# are in molar fraction.

Experiment	AK02_04		T19_01		T19_03		T19_04		AK05_01		AK05_02		AK05_03		AK05_05		AK06_01		AK06_02		AK08_03	
P (GPa)	0.4		0.8		0.8		0.8		0.4		0.4		0.4		0.4		0.4		0.4		0.4	
T (°C)	925		850		850		850		825		825		825		825		725		725		725	
SL																						
Analysis	14		7		7		7		9		10		8		8		12		16		11	
		s.d.		s.d.		s.d.		s.d.		s.d.		s.d.		s.d.		s.d.		s.d.		s.d.		s.d.
SiO_2	42.29	0.62	51.45	0.63	44.92	0.47	49.30	1.03	49.93	0.38	47.64	0.99	44.23	0.90	41.31	0.75	47.42	0.66	47.64	0.44	49.25	0.69
TiO_2	1.42	0.11	0.68	0.06	0.81	0.06	0.59	0.06	bdl	-	0.52	0.06	0.61	0.04	bdl	-	bdl	-	bdl	-	bdl	-
Al_2O_3	14.91	0.37	19.28	0.36	17.08	0.26	19.08	0.46	18.44	0.45	18.44	0.20	17.16	0.29	18.05	0.22	18.10	0.17	15.97	0.21	18.48	0.32
FeO	6.32	0.29	3.24	0.20	3.70	0.23	2.84	0.25	3.87	0.16	3.18	0.16	3.77	0.18	3.19	0.20	2.41	0.11	3.35	0.17	2.41	0.19
MnO	bdl	-	bdl	-	bdl	-	bdl	-	bdl	-	bdl	-	bdl	-	bdl	-	bdl	-	bdl	-	0.06	0.11
MgO	0.88	0.04	0.27	0.01	0.57	0.04	0.30	0.04	0.13	0.04	0.31	0.02	0.42	0.04	0.50	0.03	0.19	0.02	0.18	0.02	0.12	0.02
CaO	10.11	0.12	1.24	0.04	3.02	0.10	1.34	0.19	1.75	0.30	1.41	0.05	2.76	0.08	2.89	0.10	0.74	0.06	0.61	0.03	1.10	0.05
Na_2O	9.14	0.18	10.24	0.36	9.78	0.35	10.21	0.19	10.54	0.25	10.62	0.54	10.57	0.26	10.33	0.52	12.55	0.28	9.60	0.18	9.49	0.83
K_2O	4.05	0.15	6.01	0.18	4.85	0.15	5.76	0.24	6.37	0.17	5.43	0.21	5.03	0.11	5.16	0.11	4.49	0.14	8.35	0.25	4.65	0.12
P_2O5	bdl	-	bdl	-	bdl	-	bdl	-	-	-	bdl	-	bdl	-	bdl	-	bdl	-	bdl	-	bdl	-
BaO	bdl	-	bdl	-	bdl	-	bdl	-	bdl	-	bdl	-	bdl	-	bdl	-	bdl	-	bdl	-	0.14	0.02
SrO	bdl	-	bdl	-	bdl	-	bdl	-	bdl	-	bdl	-	bdl	-	bdl	-	bdl	-	bdl	-	0.02	0.06
F	bdl	0.22	bdl	-	0.60	0.11	bdl	-	bdl	-	bdl	-	0.64	0.19	0.66	0.12	0.78	0.13	bdl	-	1.85	0.18
Cl	0.30	0.02	0.12	0.02	0.20	0.01	0.15	0.05	0.13	0.06	0.19	0.03	0.20	0.02	0.17	0.02	0.15	0.0	0.10	0.02	0.19	0.02
Total	89.42	-	92.54	-	85.53	-	89.58	-	91.15	-	87.74	-	85.39	-	82.27	-	86.84	-	85.80	-	87.76	-
Na_2O+K_2O	13.19	0.33	16.25	0.54	14.63	0.50	15.97	0.43	16.90	0.42	16.05	0.75	15.61	0.37	15.50	0.63	17.04	0.42	17.95	0.43	14.14	0.95
AI $[Al_2O-(Na_2O+K_2O)]$	-0.03		-0.03		-0.03		-0.03		-0.04		-0.04		-0.04		-0.04		-0.06		-0.07		-0.02	
ASI $[Al_2O_3/(CaO+Na_2O+K_2O)]$	0.39		0.75		0.64		0.75		0.67		0.71		0.62		0..65		0.67		0.62		0.82	
Fe # [FeO/(FeO+MgO)]	0.80		0.87		0.79		0.84		0.94		0.85		0.84		0.78		0.88		0.91		0.92	
CL																						
Analysis	8		7		6		5		11		9		6		5		2		9		9	
		s.d.		s.d.		s.d.		s.d.		s.d.		s.d.		s.d.		s.d.		s.d.		s.d.		s.d.
SiO_2	9.22	0.82	0.84	0.39	0.66	0.74	0.97	0.06	1.22	0.42	1.60	0.40	3.74	1.44	3.44	1.21	0.26	0.11	0.25	0.20	1.66	0.24
TiO_2	0.69	0.08	bdl	-	bdl	-	bdl	-	bdl	-	bdl	-	Bdl	0.03	bdl	-	-	-	-	-	bdl	-
Al_2O_3	1.19	0.11	0.08	0.02	0.25	0.17	0.14	0.02	0.09	0.02	0.27	0.23	0.58	0.30	0.62	0.30	bdl	-	bdl	0.01	0.26	0.13
FeO	4.78	0.49	3.96	1.05	1.16	0.25	3.38	0.30	2.08	0.35	2.11	0.36	2.48	0.69	1.82	0.51	1.25	0.22	0.90	0.28	2.04	0.10
MnO	bdl	-	0.63	0.12	0.68	0.16	0.68	0.15	0.46	0.07	0.57	0.09	0.59	0.15	0.41	0.13	1.33	0.36	0.67	0.14	0.44	0.10
MgO	1.31	0.11	1.86	0.34	1.38	0.44	2.16	0.13	0.49	0.25	1.48	0.38	1.39	0.50	1.53	0.55	1.89	0.28	0.62	0.12	0.99	0.07
CaO	33.87	1.10	28.48	1.48	35.60	3.05	28.53	1.61	30.48	1.50	29.00	2.51	29.41	5.73	30.81	2.32	20.87	1.04	21.90	1.27	36.86	1.08
Na_2O	6.82	2.45	14.33	1.87	10.45	2.19	14.25	1.38	16.45	1.26	16.86	0.65	14.56	2.50	9.73	0.94	20.90	1.75	21.42	1.89	12.27	0.90
K_2O	2.12	0.26	1.81	0.22	0.72	0.18	1.65	0.12	2.47	0.29	1.92	0.38	1.75	0.54	1.58	0.33	0.59	0.04	3.52	1.41	0.93	0.15
P_2O5	1.73	0.43	1.62	0.93	4.31	2.04	2.78	0.25	1.09	0.39	2.12	0.68	2.18	0.60	1.38	0.28	1.75	0.03	0.95	0.20	0.82	0.12
BaO	0.68	0.07	1.14	0.24	1.45	0.23	1.28	0.13	1.46	0.50	1.58	0.31	1.36	0.22	1.36	0.30	6.06	0.29	2.13	0.50	1.60	0.10
SrO	1.35	0.18	1.49	0.21	1.54	0.26	1.48	0.17	1.84	0.34	1.53	0.19	1.79	0.44	2.64	0.53	1.50	0.19	1.37	0.21	1.76	0.21
F	bdl	-	1.87	0.95	3.38	1.00	3.82	0.30	1.66	0.75	3.43	1.44	2.58	0.65	1.74	0.41	5.60	1.45	2.23	0.74	14.93	0.68
Cl	0.65	0.26	0.45	0.10	0.19	0.12	0.41	0.05	0.33	0.20	0.31	0.14	0.16	0.12	0.10	0.05	0.25	0.01	0.34	0.14	0.30	0.06
Total	64.41	-	58.57	-	61.78	-	61.54	-	60.13	-	62.76	-	62.59	-	57.16	-	62.26	-	56.31	-	74.87	-
Na_2O+K_2O	8.94	2.71	16.15	2.09	11.17	2.36	15.90	1.50	18.92	1.54	18.78	1.03	16.31	3.04	11.30	1.27	21.48	1.79	24.94	3.30	13.20	1.05

Table 3. Continued

Experiment	T14_01#		T14_02#		T16_01#		T16_02#		T18_01#		T18_03#		T18_04#		T17_01#		T17_02#		T17_04#		AK02_01*		AK02_02*	
P (GPa)	0.8		0.8		0.8		0.8		1.5		1.5		1.5		0.8		0.8		0.8		0.4		0.4	
T (°C)	975		975		950		950		925		925		925		925		925		925		925		925	
SL																								
Analysis	4		3		5		5		7		6		5		6		6		5		6		6	
		s.d.		s.d.		s.d.		s.d.		s.d.		s.d.		s.d.		s.d.		s.d.		s.d.		s.d.		s.d.
La	66.3	9.0	46.7	1.6	74.2	1.4	100.4	3.3	6.2	0.5	21.6	0.7	14.1	0.4	45.9	2.2	37.9	3.0	74.7	0.5	47.9	1.1	34.8	0.8
Ce	68.1	9.8	49.1	1.5	85.7	1.6	114.8	3.5	8.7	1.0	28.0	0.9	18.7	0.4	53.8	1.2	46.3	3.0	85.6	0.5	56.6	1.5	41.9	0.9
Pr	36.0	1.6	28.9	1.5	50.9	1.1	69.8	2.0	5.3	0.4	17.2	0.6	11.5	0.2	30.4	0.7	27.9	1.5	50.5	0.2	34.0	1.6	24.6	0.4
Nd	35.7	1.7	27.1	0.5	56.6	1.1	77.4	2.2	5.5	0.9	18.3	0.7	12.4	0.3	33.1	0.5	30.3	1.3	57.4	0.7	38.9	1.9	26.4	0.9
Sm	22.6	0.7	17.3	2.3	53.3	1.4	72.2	2.2	6.1	0.7	19.2	0.9	12.4	0.2	26.8	1.1	29.2	1.3	52.4	0.4	37.5	2.6	25.2	1.3
Eu	20.4	0.2	15.1	0.9	57.3	1.6	77.0	2.0	6.5	0.4	21.3	0.6	15.4	0.3	29.3	1.3	32.1	1.4	56.0	0.4	38.8	2.5	26.3	0.5
Tb	12.4	1.1	10.8	0.4	51.1	1.6	65.0	2.1	6.1	0.6	18.4	0.5	13.3	0.3	20.0	2.2	31.5	0.9	48.6	0.3	34.1	1.6	25.9	0.7
Dy	13.1	1.0	11.3	0.3	58.5	1.7	78.1	2.7	8.2	0.3	24.1	1.0	17.9	0.1	22.3	3.4	39.4	1.8	57.5	0.4	41.4	1.5	32.7	0.9
Y	15.5	1.1	13.0	0.2	66.1	1.8	84.7	3.1	10.0	0.6	28.0	0.9	20.8	0.2	27.6	4.5	47.7	3.2	66.2	0.4	46.4	1.6	41.2	1.5
Ho	11.5	1.1	10.2	0.2	58.9	1.9	78.3	3.0	8.9	0.7	24.4	1.0	18.2	0.2	21.2	4.0	41.5	2.2	57.9	0.4	41.7	1.7	34.7	0.7
Er	10.3	1.2	9.4	0.1	55.9	1.9	73.5	3.0	10.0	0.8	25.7	0.9	19.6	0.4	20.0	3.8	41.3	3.0	54.3	0.4	42.0	2.3	34.8	1.1
Yb	11.7	1.3	10.8	0.6	60.2	2.6	76.6	3.1	12.9	1.2	30.3	1.1	24.5	0.3	22.6	4.9	47.3	4.5	58.2	0.3	50.8	2.5	43.8	0.3
Lu	11.3	0.9	10.3	0.2	53.2	2.0	65.4	2.8	11.6	0.8	27.3	0.9	22.7	0.1	21.1	4.4	41.8	4.5	51.8	0.2	40.9	1.6	37.7	0.6
Nb	256.5	6.7	307.7	10.6	265.2	11.6	378.9	22.5	309.3	20.8	349.3	10.0	331.0	9.4	261.8	17.8	324.6	23.7	256.5	2.1	203.0	19.4	158.5	7.4
Mn	1577.4	113.0	1377.5	62.9	1948.3	26.7	1809.8	22.6	681.5	38.0	1423.2	41.1	1255.8	58.0	1096.7	30.3	1407.9	46.2	1637.4	7.6	1918.5	65.8	1260.1	14.0
Sr	2834.9	37.6	1990.0	15.8	3133.7	47.2	3270.7	30.7	526.7	34.9	1451.7	41.0	1124.4	13.2	1928.0	83.8	1298.5	92.9	3330.1	14.9	2337.2	73.9	1375.7	21.9
Ba	1849.7	57.7	1731.9	56.0	2070.6	54.2	2259.3	81.1	711.3	55.2	1648.2	52.7	1555.3	48.1	1606.8	123.1	1171.2	74.1	2095.1	8.2	1691.9	64.4	1350.9	18.5
CL																								
Analysis	5		3		5		5		5		6		5		4		5		5		10		7	
		s.d.		s.d.		s.d.		s.d.		s.d.		s.d.		s.d.		s.d.		s.d.		s.d.		s.d.		s.d.
La	282.2	41.9	294.1	13.4	173.1	5.1	158.8	11.3	216.5	7.7	181.4	13.7	226.0	6.4	267.3	21.5	207.6	7.8	175.5	6.0	153.0	5.4	189.3	7.4
Ce	236.1	34.9	248.4	13.0	172.9	5.4	154.5	10.9	243.8	8.3	204.5	16.6	253.5	7.4	262.1	17.6	205.0	6.9	178.9	6.7	150.6	6.1	178.2	5.8
Pr	119.7	5.9	139.1	6.4	98.2	3.1	87.5	6.3	141.2	4.3	121.1	9.9	147.7	3.6	138.8	8.0	116.8	4.0	102.3	4.4	85.8	2.5	99.5	3.6
Nd	115.5	4.1	126.2	6.6	107.5	4.0	93.5	6.5	152.8	3.9	129.9	11.4	159.4	2.1	146.4	5.1	124.0	3.7	114.3	6.0	93.3	3.3	104.6	2.2
Sm	61.4	2.3	67.1	1.3	88.3	3.4	74.0	6.0	137.4	5.2	119.3	10.8	138.0	2.5	95.0	2.9	96.8	3.1	94.8	3.9	76.7	3.1	80.5	1.3
Eu	50.7	2.5	55.0	3.0	91.0	3.0	77.0	4.7	130.3	2.5	123.5	11.6	156.1	3.7	93.2	6.8	103.5	2.6	96.8	4.5	78.0	3.6	85.4	2.2
Tb	25.8	3.6	29.8	1.3	71.7	2.6	53.3	4.2	109.7	3.9	96.7	8.8	120.9	2.7	48.9	7.1	79.7	2.4	76.9	4.8	58.0	3.0	65.7	1.3
Dy	24.3	3.4	27.8	1.3	75.8	3.1	58.4	4.6	135.3	5.4	117.5	10.3	147.4	2.5	47.2	8.8	87.0	2.6	86.0	4.9	65.7	3.5	74.0	1.3
Y	29.2	4.4	33.0	1.4	85.0	2.7	63.4	4.9	153.5	6.9	132.1	11.3	164.3	3.7	57.1	10.1	101.4	3.4	98.8	6.0	75.1	3.9	89.8	5.7
Ho	20.1	3.5	23.5	1.0	72.0	2.9	54.5	4.2	131.3	4.3	111.8	10.0	140.8	2.2	39.8	8.4	83.0	2.5	82.7	5.4	61.9	3.7	72.2	3.1
Er	16.0	3.5	19.0	1.0	62.7	2.6	46.6	3.7	128.3	5.6	108.2	9.4	136.1	3.4	33.1	7.9	71.8	2.1	72.7	5.2	55.2	3.4	63.7	2.4
Yb	14.5	3.3	16.3	0.6	55.1	1.6	38.6	3.2	123.6	3.9	103.5	9.4	134.0	3.4	28.4	6.8	60.2	2.4	68.3	5.7	53.6	3.9	59.2	2.1
Lu	13.0	3.0	14.1	0.6	46.1	1.1	31.1	2.3	105.3	4.2	89.7	8.1	116.1	3.4	24.8	6.0	48.4	2.1	57.7	5.3	42.9	2.9	48.1	1.5
Nb	190.7	42.8	175.0	34.2	187.0	22.5	177.5	21.6	289.1	42.8	298.5	111.3	239.5	129.6	192.7	34.4	205.9	5.9	210.3	18.9	165.7	16.0	117.4	6.0
Mn	2725.6	309.3	2751.2	64.3	2396.0	261.9	1433.4	98.4	5081.0	257.7	4180.7	462.0	4999.0	113.8	2208.9	172.6	2629.3	193.0	2196.1	83.8	2461.3	166.6	2176.0	117.4
Sr	14819.6	370.1	14893.4	76.4	10401.9	201.7	11611.4	228.3	8766.1	105.6	8008.9	205.3	9589.7	157.7	12561.0	501.3	11273.9	238.2	9713.8	158.0	9041.1	343.1	10275.0	107.3
Ba	6693.7	208.8	7883.9	292.6	5399.7	403.1	6127.5	269.8	6395.9	240.2	6935.7	814.0	8501.5	321.2	6603.6	283.8	6369.1	593.5	4618.8	191.5	4296.3	323.2	5888.0	466.7

Table 4. Trace elements concentrations of experimental silicate and carbonate liquids (µg/g, i.e. ppm) measured by LA-ICP-MS. SL: silicate liquid; CL: carbonate liquid; bdl: below detection limit; s.d.: standard deviation, statistical uncertainty calculated on the mean value; *: sample analysed by the Thermo Element XR ICP-MS; #: sample analysed by the Agilent 7500 CS ICP-MS.

Experiment	AK02_04*		T19_01*,#		T19_03#		T19_04*		AK05_01*		AK05_02#		AK05_03#		AK05_05#		AK06_01*		AK06_02*		AK08_03*	
P (GPa)	0.4		0.8		0.8		0.8		0.4		0.4		0.4		0.4		0.4		0.4		0.4	
T (°C)	925		850		850		850		825		825		825		825		725		725		725	
SL																						
Analysis	6		10		8		10		14		9		7		9		11		11		7	
		s.d.		s.d.		s.d.		s.d.		s.d.		s.d.		s.d.		s.d.		s.d.		s.d.		s.d.
La	58.9	1.5	5.8	0.5	21.4	0.7	7.3	1.9	16.8	1.7	14.6	0.8	31.8	1.6	38.9	1.0	11.0	0.9	6.1	0.2	8.59	0.56
Ce	69.1	1.5	7.5	0.9	26.1	0.8	9.3	2.1	22.2	2.2	17.4	0.9	37.1	1.5	40.8	1.2	13.0	0.7	7.9	0.2	10.78	0.55
Pr	39.6	0.9	4.3	0.3	13.9	0.4	5.0	1.0	12.3	1.2	9.9	0.4	20.0	0.8	19.0	0.8	6.1	0.3	4.3	0.1	6.03	0.59
Nd	43.9	1.1	4.3	0.5	15.5	0.6	5.3	1.0	13.5	1.3	10.8	0.5	20.9	0.8	14.2	1.0	6.3	0.6	4.8	0.2	6.34	0.81
Sm	39.1	0.9	4.6	0.6	14.5	0.5	5.3	0.8	14.3	1.4	10.9	0.5	18.6	1.0	5.4	0.8	6.5	0.5	4.9	0.3	6.34	1.01
Eu	42.6	0.7	5.1	0.7	19.0	0.5	5.8	0.7	16.4	1.7	11.6	0.6	20.2	0.9	3.5	0.6	7.8	0.4	5.1	0.2	6.75	0.70
Tb	34.0	0.4	5.2	0.5	15.3	0.1	6.1	0.7	16.5	1.5	12.7	0.7	18.9	1.2	1.8	0.5	9.5	0.6	5.3	0.2	7.37	0.45
Dy	43.1	0.8	7.1	1.0	20.9	0.2	7.7	1.1	22.6	1.8	17.4	1.1	24.4	1.6	1.5	0.5	12.7	1.1	6.9	0.2	10.51	0.95
Y	51.2	0.9	9.6	1.5	27.1	0.3	10.4	1.6	29.9	1.8	24.7	1.8	33.5	2.2	1.8	0.5	20.8	1.9	10.3	0.5	15.96	1.60
Ho	43.1	0.6	8.0	1.3	23.5	0.3	8.6	1.2	25.2	2.0	19.4	1.2	26.7	1.8	1.3	0.4	15.5	1.2	7.9	0.5	12.15	0.96
Er	41.9	0.8	9.0	1.6	25.3	0.4	9.7	1.4	26.3	2.2	22.2	1.6	28.0	1.9	1.2	0.4	17.6	1.4	8.5	0.6	13.76	0.97
Yb	48.2	1.0	13.6	2.5	35.3	0.4	14.4	2.1	33.6	2.5	32.0	1.7	36.6	2.5	1.7	0.5	24.9	2.0	12.6	0.9	21.45	1.41
Lu	40.7	0.6	12.5	2.3	32.7	0.4	13.0	1.5	28.0	2.3	27.6	1.1	32.5	1.9	1.9	0.4	24.7	1.9	12.3	0.8	20.39	1.55
Nb	228.6	5.6	120.6	16.3	150.2	1.8	145.2	11.2	225.8	48.4	138.8	10.4	186.3	8.5	66.0	5.7	60.5	3.5	80.8	1.6	76.06	5.10
Mn	1513.7	14.2	622.9	35.8	1142.6	19.3	669.2	26.4	807.5	26.1	966.9	18.0	1416.3	40.1	1091.3	31.3	719.8	32.2	636.5	12.9	536.90	28.88
Sr	2433.5	54.3	408.5	10.4	1154.9	19.3	465.8	10.8	560.1	36.0	672.5	7.6	1295.1	10.5	1930.8	43.9	241.9	6.7	169.3	2.9	376.62	17.40
Ba	1662.9	48.3	685.3	25.7	1799.2	34.0	909.8	61.1	901.1	101.7	1419.8	24.6	1808.6	39.4	1808.2	51.2	1162.0	32.0	508.2	11.9	823.70	39.25
CL																						
Analysis	10		7		5		9		11		8		6		9		2		11		5	
		s.d.		s.d.		s.d.		s.d.		s.d.		s.d.		s.d.		s.d.		s.d.		s.d.		s.d.
La	150.5	9.5	168.0	19.2	338.4	40.0	195.7	11.9	198.6	34.2	336.4	29.4	391.2	34.4	459.8	30.2	447.7	60.1	298.3	26.0	376.79	10.01
Ce	151.9	10.8	160.7	20.2	349.5	44.0	190.0	10.3	194.4	27.3	330.7	27.3	376.0	27.9	410.9	17.8	394.0	79.1	278.1	16.0	345.24	7.41
Pr	85.3	5.5	92.0	6.5	173.7	22.7	105.4	5.2	103.8	13.0	167.7	17.0	189.4	16.8	174.6	10.0	193.7	39.7	154.5	9.4	177.62	4.43
Nd	91.8	4.9	92.9	7.9	192.7	29.2	112.1	5.4	109.9	13.4	178.2	19.6	188.9	14.3	126.8	7.4	205.2	40.5	160.6	7.3	172.92	4.75
Sm	73.5	3.9	76.0	3.8	156.8	25.4	92.9	5.2	90.6	8.6	144.7	19.2	142.9	13.5	42.0	5.2	170.5	35.2	128.8	6.5	131.33	2.96
Eu	76.4	4.0	76.6	7.4	187.9	29.0	89.8	5.1	91.6	8.8	138.2	19.0	140.5	10.2	25.3	4.3	171.8	49.7	117.8	8.3	135.62	4.30
Tb	54.2	2.8	65.4	5.9	133.2	18.7	82.3	5.9	71.3	8.4	121.5	19.5	112.7	12.5	11.0	2.6	160.5	44.5	93.6	6.7	110.25	4.87
Dy	63.3	3.7	72.0	4.4	168.6	27.1	90.7	5.8	83.2	9.9	142.1	24.8	128.5	12.5	8.7	2.5	181.2	49.2	101.9	8.7	132.31	5.40
Y	74.8	4.1	93.1	7.9	202.4	22.3	115.7	8.1	105.0	15.2	182.7	35.6	162.9	22.3	10.1	2.8	304.1	28.4	130.8	15.0	201.86	5.12
Ho	60.4	3.0	72.6	4.8	171.6	21.6	90.5	6.3	82.5	10.4	143.3	26.2	132.0	9.9	6.7	1.9	188.4	58.1	97.8	9.4	137.21	3.94
Er	54.2	2.0	67.5	5.5	164.7	19.5	87.2	6.4	73.3	9.9	139.5	26.4	117.1	13.4	5.4	1.6	184.8	52.9	86.3	9.7	130.20	7.56
Yb	51.2	2.5	71.3	5.6	174.6	19.5	90.9	6.5	65.3	8.9	140.9	27.2	113.3	10.2	5.7	1.1	173.3	61.2	80.2	14.0	136.36	4.62
Lu	41.9	1.7	62.2	4.2	165.9	52.9	76.6	5.5	49.6	8.7	110.1	21.3	90.0	9.5	5.9	1.0	153.4	47.4	67.7	14.3	115.66	3.49
Nb	198.6	14.9	49.9	10.6	119.8	50.9	108.9	28.7	81.2	20.9	130.0	47.3	217.8	71.0	67.1	26.4	65.5	59.8	40.6	31.7	45.74	5.54
Mn	1893.7	202.6	2847.6	269.9	5073.0	1249.5	4097.3	725.8	2171.8	342.4	5009.3	1527.0	5300.7	1272.3	3386.3	342.3	5992.5	328.2	3306.8	573.5	1959.60	35.83
Sr	8546.0	310.6	8770.3	269.2	12226.5	431.4	9396.7	173.6	10290.2	641.8	11510.0	373.9	12684.2	745.6	18679.0	650.9	6332.5	734.6	6858.4	222.2	10768.41	116.42
Ba	4152.7	130.2	5556.7	563.0	14120.7	3881.9	8848.6	1122.0	7748.4	1570.0	15519.7	3286.1	14127.1	2652.9	11181.4	692.9	21634.4	3207.1	10457.9	1336.1	9132.87	183.06

Table 4. Continued

Experiment	T14_01		T14_02		T16_01		T16_02		T18_01		T18_03		T18_04		T17_01		T17_02		T17_04		AK02_01		AK02_02	
P (GPa)	0.8		0.8		0.8		0.8		1.5		1.5		1.5		0.8		0.8		0.8		0.4		0.4	
T (°C)	975		975		950		950		925		925		925		925		925		925		925		925	
		s.d.		s.d.		s.d.		s.d.		s.d.		s.d.		s.d.		s.d.		s.d.		s.d.		s.d.		s.d.
Ca	5.08	0.34	7.62	0.70	3.27	0.14	3.29	0.60	16.75	0.35	6.11	1.08	10.34	0.66	6.77	0.81	8.07	1.19	3.12	0.34	3.91	0.23	7.38	0.59
La	4.26	0.86	6.30	0.36	2.33	0.08	1.58	0.12	34.76	3.14	8.41	0.70	16.05	0.67	5.83	0.55	5.47	0.48	2.35	0.08	3.19	0.13	5.43	0.24
Ce	3.47	0.71	5.06	0.31	2.02	0.07	1.35	0.10	27.88	3.30	7.31	0.64	13.59	0.49	4.87	0.34	4.43	0.32	2.09	0.08	2.66	0.13	4.25	0.17
Pr	3.33	0.22	4.81	0.33	1.93	0.07	1.25	0.10	26.72	2.24	7.05	0.63	12.89	0.41	4.57	0.28	4.18	0.27	2.03	0.09	2.52	0.14	4.05	0.16
Nd	3.24	0.19	4.64	0.26	1.90	0.08	1.21	0.09	27.55	4.47	7.11	0.68	12.87	0.39	4.42	0.17	4.09	0.22	1.99	0.11	2.40	0.15	3.96	0.15
Sm	2.71	0.13	3.88	0.53	1.66	0.08	1.02	0.09	22.61	2.72	6.20	0.63	11.14	0.28	3.54	0.19	3.31	0.19	1.81	0.08	2.05	0.17	3.19	0.17
Eu	2.48	0.13	3.64	0.29	1.59	0.07	1.00	0.07	20.04	1.36	5.80	0.57	10.16	0.31	3.18	0.27	3.22	0.16	1.73	0.08	2.01	0.16	3.24	0.10
Tb	2.08	0.34	2.76	0.16	1.40	0.07	0.82	0.07	17.85	1.80	5.26	0.50	9.11	0.27	2.45	0.45	2.53	0.11	1.58	0.10	1.70	0.12	2.54	0.09
Dy	1.85	0.30	2.46	0.13	1.30	0.06	0.75	0.06	16.45	0.89	4.87	0.47	8.26	0.15	2.11	0.51	2.21	0.12	1.50	0.09	1.59	0.10	2.26	0.08
Y	1.88	0.31	2.54	0.12	1.29	0.05	0.75	0.06	15.32	1.20	4.72	0.43	7.89	0.20	2.07	0.50	2.13	0.16	1.49	0.09	1.62	0.10	2.18	0.16
Ho	1.75	0.35	2.31	0.11	1.22	0.06	0.70	0.06	14.77	1.30	4.58	0.45	7.72	0.14	1.87	0.53	2.00	0.12	1.43	0.09	1.48	0.11	2.08	0.10
Er	1.56	0.39	2.01	0.11	1.12	0.06	0.63	0.06	12.87	1.13	4.21	0.39	6.95	0.22	1.65	0.50	1.74	0.14	1.34	0.10	1.31	0.11	1.83	0.09
Yb	1.24	0.31	1.51	0.09	0.92	0.05	0.50	0.05	9.57	0.90	3.41	0.33	5.47	0.16	1.26	0.41	1.27	0.13	1.17	0.10	1.05	0.09	1.35	0.05
Lu	1.15	0.29	1.37	0.07	0.87	0.04	0.48	0.04	9.08	0.69	3.29	0.31	5.12	0.15	1.18	0.38	1.16	0.13	1.11	0.10	1.05	0.08	1.28	0.05
Nb	0.74	0.17	0.57	0.11	0.71	0.09	0.47	0.06	0.93	0.15	0.85	0.32	0.72	0.39	0.74	0.14	0.63	0.05	0.82	0.07	0.82	0.11	0.74	0.05
Mn	1.73	0.23	2.00	0.10	1.23	0.14	0.79	0.06	7.46	0.56	2.94	0.34	3.98	0.20	2.01	0.17	1.87	0.15	1.34	0.05	1.28	0.10	1.73	0.10
Sr	5.23	0.15	7.48	0.07	3.32	0.08	3.55	0.08	16.64	1.12	5.52	0.21	8.53	0.17	6.52	0.38	8.68	0.65	2.92	0.05	3.87	0.19	7.47	0.14
Ba	3.62	0.16	4.55	0.22	2.61	0.21	2.71	0.15	8.99	0.77	4.21	0.51	5.47	0.27	4.11	0.36	5.44	0.61	2.20	0.09	2.54	0.21	4.36	0.35

Experiment	AK02_04		T19_01		T19_03		T19_04		AK05_01		AK05_02		AK05_03		AK05_05		AK06_01		AK06_02		AK08_03	
P (GPa)	0.4		0.8		0.8		0.8		0.4		0.4		0.4		0.4		0.4		0.4		0.4	
T (°C)	925		850		850		850		825		825		825		825		725		725		725	
		s.d.		s.d.		s.d.		s.d.		s.d.		s.d.		s.d.		s.d.		s.d.		s.d.		s.d.
Ca	3.35	0.12	23.00	1.42	11.80	1.09	21.25	3.26	17.37	3.05	20.55	1.91	10.67	2.10	10.67	0.88	28.24	2.62	35.83	2.86	33.44	1.70
La	2.56	0.17	28.78	4.09	15.82	1.95	26.98	7.09	11.82	2.34	23.01	2.35	12.30	1.25	11.82	0.87	40.83	6.46	48.94	4.44	43.87	3.09
Ce	2.20	0.16	21.39	3.65	13.40	1.73	20.47	4.75	8.76	1.52	18.96	1.83	10.13	0.86	10.07	0.53	30.31	6.29	35.04	2.27	32.02	1.77
Pr	2.15	0.15	21.39	2.28	12.53	1.67	21.24	4.36	8.41	1.34	16.94	1.87	9.46	0.92	9.21	0.64	31.62	6.63	35.82	2.30	29.47	2.99
Nd	2.09	0.12	21.41	3.16	12.41	1.94	21.25	4.11	8.16	1.28	16.56	1.99	9.05	0.77	8.91	0.82	32.36	7.12	33.69	1.98	27.27	3.54
Sm	1.88	0.11	16.49	2.27	10.79	1.79	17.45	2.75	6.33	0.87	13.32	1.89	7.68	0.84	7.79	1.45	26.40	5.81	26.37	2.21	20.70	3.34
Eu	1.79	0.10	15.02	2.49	9.88	1.55	15.60	2.02	5.58	0.78	11.95	1.74	6.96	0.60	7.15	1.67	21.99	6.46	23.18	1.82	20.10	2.19
Tb	1.59	0.08	12.55	1.68	8.68	1.22	13.39	1.82	4.33	0.65	9.55	1.62	5.97	0.76	6.22	2.17	16.98	4.83	17.55	1.46	14.96	1.13
Dy	1.47	0.09	10.13	1.59	8.07	1.30	11.83	1.85	3.68	0.53	8.16	1.52	5.27	0.62	5.71	2.44	14.26	4.06	14.71	1.36	12.58	1.25
Y	1.46	0.08	9.71	1.72	7.46	0.83	11.08	1.87	3.51	0.55	7.38	1.54	4.86	0.74	5.57	2.19	14.61	1.92	12.74	1.60	12.65	1.30
Ho	1.40	0.07	9.05	1.60	7.30	0.93	10.54	1.68	3.27	0.49	7.40	1.43	4.95	0.50	5.18	2.17	12.19	3.87	12.42	1.39	11.29	0.95
Er	1.29	0.05	7.51	1.44	6.51	0.78	8.96	1.43	2.78	0.44	6.30	1.28	4.18	0.56	4.66	2.21	10.50	3.12	10.18	1.33	9.46	0.87
Yb	1.06	0.06	5.24	1.06	4.95	0.56	6.34	1.02	1.95	0.30	4.40	0.88	3.10	0.35	3.37	1.18	6.96	2.52	6.38	1.20	6.36	1.61
Lu	1.03	0.04	4.98	0.97	5.07	1.62	5.87	0.78	1.77	0.34	3.99	0.79	2.77	0.33	3.14	0.92	6.21	1.98	5.51	1.22	5.67	0.47
Nb	0.87	0.07	0.41	0.10	0.80	0.34	0.75	0.21	0.36	0.12	0.94	0.35	1.17	0.38	1.02	0.41	1.08	0.99	0.50	0.39	0.60	0.08
Mn	1.25	0.13	4.57	0.51	4.44	1.10	6.12	1.11	2.69	0.43	5.18	1.58	3.74	0.90	3.10	0.33	8.32	0.59	5.20	0.91	3.65	0.21
Sr	3.51	0.15	21.47	0.86	10.59	0.41	20.17	0.60	18.37	1.65	17.11	0.59	9.79	0.58	9.67	0.40	26.18	3.12	40.50	1.48	28.59	1.36
Ba	2.50	0.11	8.11	0.88	7.85	2.16	9.73	1.40	8.60	1.99	10.93	2.32	7.81	1.48	6.18	0.42	18.62	2.81	20.58	2.67	11.09	0.57

Table 5. Trace elements and calcium partition coefficients between silicate and carbonate liquids. s.d.: standard deviation, calculated statistical uncertainty.

				Silicate melt wt %		wt % - Volatile-free basis		Molar fractions			
Study	N	P (GPa)	T (°C)	SiO_2	CaO	SiO_2	CaO	AI $[Al_2O_3-(Na_2O+K_2O)]$	ASI $[Al_2O_3/(CaO+Na_2O+K_2O)]$	Measured $D_{Ca}^{CL/SL}$	Calculated $D_{Ca}^{CL/SL}$
This study *	23	0.4 - 1.5	725 - 975	38.9 - 52.1	0.6 - 11.5	44.8 - 55.7	0.7 - 13.2	-0.07 to -0.01	0.33 – 0.82	3.1 - 35.8	2.6 - 42.1
Brooker 1998	16	2.5	1250 - 1300	23.8 - 52.7	0.8 - 22.8	28.8 - 56.4	0.8 - 29.0	-0.35 to -0.03	0.07 – 0.84	1.0 - 8.5	0.9 - 7.5
Freestone and Hamilton 1980	8	0.07 - 0.76	995 - 1100	33.8 - 51.9	2.3 - 24.5	37.1 - 53.2	2.4 - 26.9	-0.15 to -0.07	0.15 – 0.52	1.0 - 7.6	1.3 - 10.6
Hamilton et al. 1989 *	15	0.08 - 0.6	1050 - 1250	31.9 - 50.5	3.0 - 24.6	35.6 - 52.6	3.2 - 27.5	-0.17 to -0.05	0.15 – 0.49	1.0 - 8.4	1.2 - 8.8
Jones et al. 1995	2	1	1250	28.5 - 33.6	19.8 - 24.2	33.4 - 38.2	22.5 - 28.4	-0.09 to -0.08	0.15 – 0.19	1.3 - 1.5	1.0 - 1.4
Kjarsgaard et al. 1995	7	0.106 - 0.38	700 - 850	40.1 - 50.1	1.0 - 5.5	46.3 - 54.2	1.1 - 6.4	-0.11 to -0.07	0.40 – 0.63	4.9 - 23.8	3.9 - 25.3
Kjarsgaard 1998	9	0.19 - 0.515	900 - 1025	37.8 - 52.1	1.8 - 15.2	42.6 - 54.4	1.9 - 17.1	-0.05 to -0.03	0.27 – 0.73	2.5 - 18.4	2.0 - 17.4
Martin et al. 2012	7	1.7	1220	32.8 - 47.8	7.6 - 18.0	38.2 - 50.6	8.0 - 21.0	-0.01 to 0.03	0.25 – 0.60	1.8 - 4.9	1.5 - 5.7
Martin et al. 2013 *	19	1 - 3.2	1150 - 1260	26.3 - 64.1	1.0 - 25.6	31.4 - 69.0	1.1 - 30.6	-0.08 to -0.01	0.06 – 0.84	1.2 - 24.2	0.8 - 30.1
Massuyeau et al. 2015	8	3	1300 - 1400	40.6 - 56.3	1.5 - 18.0	45.8 - 60.8	1.5 - 20.2	-0.06 to -0.01	0.32 – 0.69	1.9 - 13.2	2.3 - 11.0
Veksler et al. 1998	3	0.04 - 0.09	965 - 1015	53.3 - 57.6	3.9 - 8.0	53.6 - 58.8	4.0 - 8.2	-0.22 to -0.18	0.14 – 0.18	1.7 - 2.6	3.3 - 4.3
Veksler et al. 2012 *	4	0.1	850 - 950	38.8 - 57.3	3.0 - 7.0	45.3 - 60.6	3.2 - 8.2	-0.16 to -0.12	0.23 – 0.33	1.4 - 3.6	3.0 - 5.4

Table 6. Experimental database of immiscible carbonate and silicate melts used for the modelling of carbonatite REE compositions. All studies were used for the $D_{Ca}^{CL/SL}$ calculation. Only the studies with * were used for the $D_{REE}^{CL/SL}$-$D_{Ca}^{CL/SL}$ modelling and carbonatite REE composition calculation. N: number of experiments; P: pressure; T: temperature; SL: silicate liquid; CL: carbonate liquid; SiO_2 and CaO contents of the silicate melts or in wt %. AI (alkalinity index) and ASI (alumina saturation index) of the silicate melts are in molar fractions.

a. $D_{Ca}^{CL/SL}$ modelling

$Ln(D_{Ca}^{CL/SL}) = a_0 + a_1 * SiO_2 + a_2 * Al_2O_3 / (CaO+Na_2O+K_2O) + a_3 * (Na_2O+K_2O)/(CaO+MgO)$

a_0	-1.645	σ error (a_0)	0.103
a_1	4.157	σ error (a_1)	0.276
a_2	1.482	σ error (a_2)	0.144
a_3	0.116	σ error (a_3)	0.007

b. $D_{REE}^{CL/SL} - D_{Ca}^{CL/SL}$ modelling

$D_{REE}^{CL/SL} = a * [(D_{Ca}^{CL/SL}) \wedge b]$

	a	σ error (a)	b	σ error (b)
La	0.536	0.039	1.325	0.037
Ce	0.496	0.037	1.300	0.043
Pr	0.507	0.047	1.265	0.005
Nd	0.509	0.049	1.241	0.057
Sm	0.471	0.049	1.225	0.056
Eu	0.446	0.044	1.233	0.054
Gd	0.508	0.068	1.171	0.073
Tb	0.498	0.055	1.088	0.060
Dy	0.418	0.067	1.175	0.082
Y	0.425	0.057	1.192	0.069
Ho	0.210	0.072	1.431	0.162
Er	0.420	0.058	1.097	0.073
Yb	0.339	0.052	1.127	0.078
Lu	0.356	0.050	1.074	0.075

Table 7. Calculated coefficients and associated errors used for the modelling. a. Coefficients calculated for the $D_{Ca}^{CL/SL}$ parameterisation from the silicate liquid composition. b. Coefficients calculated from the $D_{REE}^{CL/SL}$ calculation (weighted least square regression for both calculations); SL: silicate liquid; CL: carbonate liquid.

Fig. 1. BSE images of typical carbonate-silicate liquid immiscibility textures. Silicate melts quenched into homogeneous and microlite-free glasses, while carbonate melts quenched into carbonate blebs with inter-crystallized Na-rich and Ca-rich bands, which are typical textures of unquenchable carbonate liquids (Brooker and Kjarsgaard, 2011). CL: carbonate liquid; SL: silicate liquid; Cpx: clinopyroxene; Fe-Spl: spinel; Cc: calcite; Nph: nepheline. Au: gold capsule.

Fig. 2. Crystal fractionation effect on liquids composition. Major elements compositions of liquids from this study (coloured data symbols) and previous experimental investigations (grey dots; Hamilton et al., 1989; Veksler et al., 1998; Veksler et al., 2012; Martin et al., 2013). (a) Total alkali versus SiO_2 (TAS; (Le Bas et al., 1986) diagram of immiscible carbonate and silicate liquids (a: picro-basalt; b: basalt; c: basaltic andesite; d: andesite; e: dacite; f: rhyolite; g: tephri-basanite; h: trachy-basalt; i: basaltic trachy-andesite; j: trachy-andesite; k: trachyte; l: foïdite; m: phono-tephrite; n: tephri-phonolite; o: phonolite). The silicate liquid compositions are on a volatile-free basis. Each line connects a carbonate liquid (CL) coexisting at equilibrium with a silicate liquid (SL). Error bars indicate the standard deviation. Silica content (b), alumina saturation index (b) and alkaline/alkaline earth cations ratio (c) versus the CaO contents of the silicate melt. SiO_2 and CaO contents are in wt % on a volatile free basis, and the alumina saturation index and alkaline/alkaline earth cations ratio are in molar fractions. For (b) to (d), data from this study are compared to data from Kjarsgaard (1998; grey dots) which also experimented crystal fractionation.

Fig. 3. Variation of carbonate liquid compositions during the differentiation. CaO contents versus the Na_2O contents of the carbonate liquids in wt%, for all P-T conditions. Carbonate liquids evolved from a Ca-rich pole towards a Na-rich pole along the differentiation. CL: carbonate liquid.

Fig. 4. REE behaviour between carbonate and silicate liquids. REE partition coefficients ($D_{REE}^{CL/SL}$) from this study and previous experimental investigations (grey dots; Hamilton et al., 1989; Veksler et al., 1998; Veksler et al., 2012; Martin et al., 2013). (a) Ca and REE partition coefficients measured between carbonate and silicate liquids. (c) and (d) La partition coefficients ($D_{La}^{CL/SL}$) respectively versus the wt% CaO in the silicate melts and Ca partition coefficients ($D_{Ca}^{CL/SL}$). CL: carbonate liquid; SL: silicate liquid.

Fig. 5. Ca partitioning dependence on melt compositions. We represent the measured Ca partition coefficient ($D_{Ca}^{CL/SL}$) between carbonate and silicate melts, against three terms relative to the silicate melts composition used for the $D_{Ca}^{CL/SL}$ calibration: the silica content (a), the ASI (alumina saturation index) (b) and alkali/alkaline-earth cation ratio (c) for this study (red dots) and the experimental database used for the modelling (grey dots; Freestone and Hamilton, 1980; Hamilton et al., 1989; Kjarsgaard et al., 1995; Jones et al., 1995; Brooker, 1998; Kjarsgaard, 1998; Veksler et al., 1998; Veksler et al., 2012; Martin et al., 2012; Martin et al., 2013; Massuyeau et al., 2015). CL: carbonate liquid; SL: silicate liquid.

Fig. 6. Modelling for calcium and lanthanum partition coefficients between carbonate and silicate liquids. a. Modeled Ca partition coefficients between carbonate and silicate immiscible liquids ($D_{Ca}^{CL/SL}$ calculated) represented versus the experimentally measured Ca partition coefficients ($D_{Ca}^{CL/SL}$ measured), from this study (red dots) and the immiscibility database (grey dots; Tables 6 and 7a) used for the model (Freestone and Hamilton, 1980; Hamilton et al., 1989; Kjarsgaard et al., 1995; Jones et al., 1995; Brooker, 1998; Kjarsgaard, 1998; Veksler et al., 1998; Veksler et al., 2012; Martin et al., 2012; Martin et al., 2013; Massuyeau et al., 2015). b. Modeled La partition coefficients ($D_{La}^{CL/SL}$ calculated) as representative of other REE partitioning, against measured La partitioning ($D_{La}^{CL/SL}$ measured) parameterised from this study and other experimental studies (Hamilton et al., 1989; Veksler et al., 2012; Martin et al., 2013) on REE partitioning (Tables 6 and 7b). CL: carbonate liquid; SL: silicate liquid.

Fig. 7. Modelled carbonatite REE compositions compared to the natural carbonatite and silicate rock compositions of Lofdal in Namibia. Carbonatite REE contents are calculated here from phonolite (grey triangles) and phono-tephrite (red triangles) mean compositions of the Lofdal magmatic suite in Namibia (Bodeving et al., 2017) and normalised to chondrites (McDonough and Sun, 1995). The calculated carbonatite REE concentrations (filled circles) are compared to those of the natural carbonatite from this district (open blue circles; Bodeving et al., 2017). The error bars of the two compositions are estimated from the error propagation formalism detailed in the main text. Ca partition coefficients calculated from the first step of the modelling are indicate for both calculated carbonatite REE compositions in brackets.

Fig. 8. Natural alkaline magmatic rocks from the East-African Rift and the Canary and Cape Verde Islands, and calculated composition of potential associated carbonatites. **a)** TAS diagram showing the composition of alkaline magmatic rocks (on a volatile-free basis) from the East-African Rift, the Canary Islands and the Cape Verde Islands: data from the GEOROC database and additional studies (De Moor et al., 2013; Mattsson et al., 2013; Mana et al., 2015). The colour gradient from blue to red indicates increasing values of $D_{Ca}^{CL/SL}$, calculated from the major element composition of each silicate rock, for the East-African Rift (circles), Canary Islands (triangles) and Cape Verde Islands (squares) settings. Data from the Ol Doinyo Lengai volcano in Tanzania (black arrow) follow a different trend of differentiation characterised by hyper-alkaline compositions (De Moor et al., 2013). The grey line correspond to the maximum extent of miscibility gap proposed by Schmidt and Weidendorfer (2018) which separate the field where immiscibility has been observed from the domain not investigated so far (Fig. A.4). **b)** Calculated La and Lu concentrations of potential carbonatites coexisting with alkaline magma compositions in (a), against the CaO contents (wt%) of the alkaline magmatic rocks from the three geological settings.Fig. 9. Alkaline magmatic rocks from the East African Rift and calculated carbonatite compositions normalised to chondrite. (a) Changes in the REE contents of alkaline magmatic rocks from the East African Rift across differentiation. The East-African Rift silicate magmatic rocks used to calculate carbonatite REE contents of Fig. 8 are normalised to chondrites (McDonough and Sun, 1995). The calculated Ca partition coefficient ($D_{Ca}^{CL/SL}$ calculated) is represented for each magmatic

composition by a colour gradient (data from GEOROC; De Moor et al., 2013; Mattsson et al., 2013; Mana et al., 2015). (b) Calculated carbonatite REE compositions normalised to chondrites. REE contents of carbonatites are calculated from the alkaline silicate magma compositions and are normalised to chondrite (McDonough and Sun, 1995). The anomalies in some chondrite-normalised REE profiles reflect anomalies of natural silicate rocks compositions. The profiles are characterized by a strong enrichment in LREE and a relatively slight flat distribution of HREE. The grey field represents the compositions of carbonatite REE deposits currently mined: Bayan Obo, Mianing deposits and Mountain Pass (from Verplanck et al., 2016).

Fig. 10. Alkaline magmatic rocks from the Canary and Cape Verde Islands, and calculated carbonatite compositions normalised to chondrite. (a) Changes in the REE contents of alkaline magmatic rocks from the Canary (triangles) and Cape Verde Islands (squares) across differentiation (data from GEOROC database). The silicate magmatic rocks used to calculate carbonatite REE contents of Fig. 8 are normalised to chondrites (McDonough and Sun, 1995) for boths settings. The colour gradient represent the calculated Ca partition coefficient ($D_{Ca}^{CL/SL}$ calculated) for each magmatic rocks by a. (b) Calculated carbonatite REE compositions normalised to chondrites, for the Canary and Cape Verde Islands. Carbonatite REE compositions are calculated from the alkaline silicate magmas shown in Fig. 8 and normalised to chondrite (McDonough and Sun, 1995). The chondrite-normalised REE profiles are also characterised by a strong enrichment in LREE and a relatively slight flat distribution of HREE. The grey field represents the compositions of carbonatite REE deposits currently mined: Bayan Obo, Mianing deposits and Mountain Pass (from Verplanck et al., 2016).

Fig. 11. Optimum of carbonatite REE enrichment along the alkaline magma differentiation course, for the East African Rift and Canary and Cape Verde Islands. The alkalinity index (AI = AL_2O_3-(Na_2O+K_2O)) for all the alkaline magmatic rocks of the three settings from Fig.8-9-10 is represented against their alumina saturation index (ASI = Al_2O_3 / (CaO+Na_2O+K_2O)). Both index are calculated in molar fractions. The calculated Ca partition coefficient ($D_{Ca}^{CL/SL}$ calculated) is represented for each magmatic compositions by a colour gradient. The optimum of carbonatite REE enrichment correspond to phonolitic / phono-trachytic compositions ($D_{Ca}^{CL/SL} > 20$), at the boundary between peralkaline and metaluminous domains (grey field). The hyper-alkaline rocks from the Ol Doinyo Lengai volcano (black arrow) which present a strong peralkalinity, are far from this optimum.

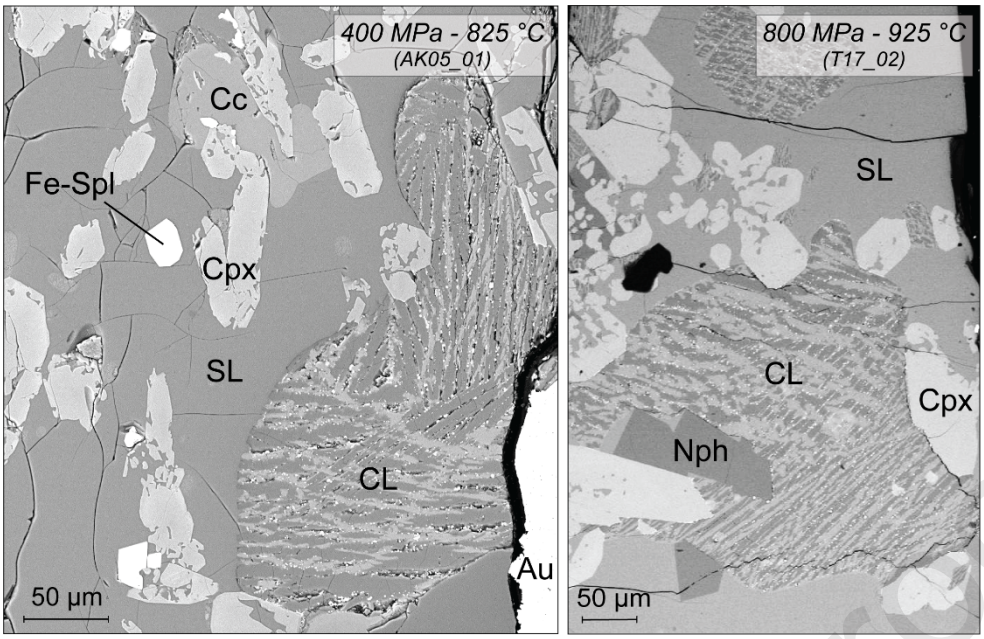

Fig. 1. BSE images of typical carbonate-silicate liquid immiscibility textures. Silicate melts quenched into homogeneous and microlite-free glasses, while carbonate melts quenched into carbonate blebs with inter-crystallized Na-rich and Ca-rich bands, which are typical textures of unquenchable carbonate liquids (Brooker and Kjarsgaard, 2011). CL: carbonate liquid; SL: silicate liquid; Cpx: clinopyroxene; Fe-Spl: spinel; Cc: calcite; Nph: nepheline. Au: gold capsule.

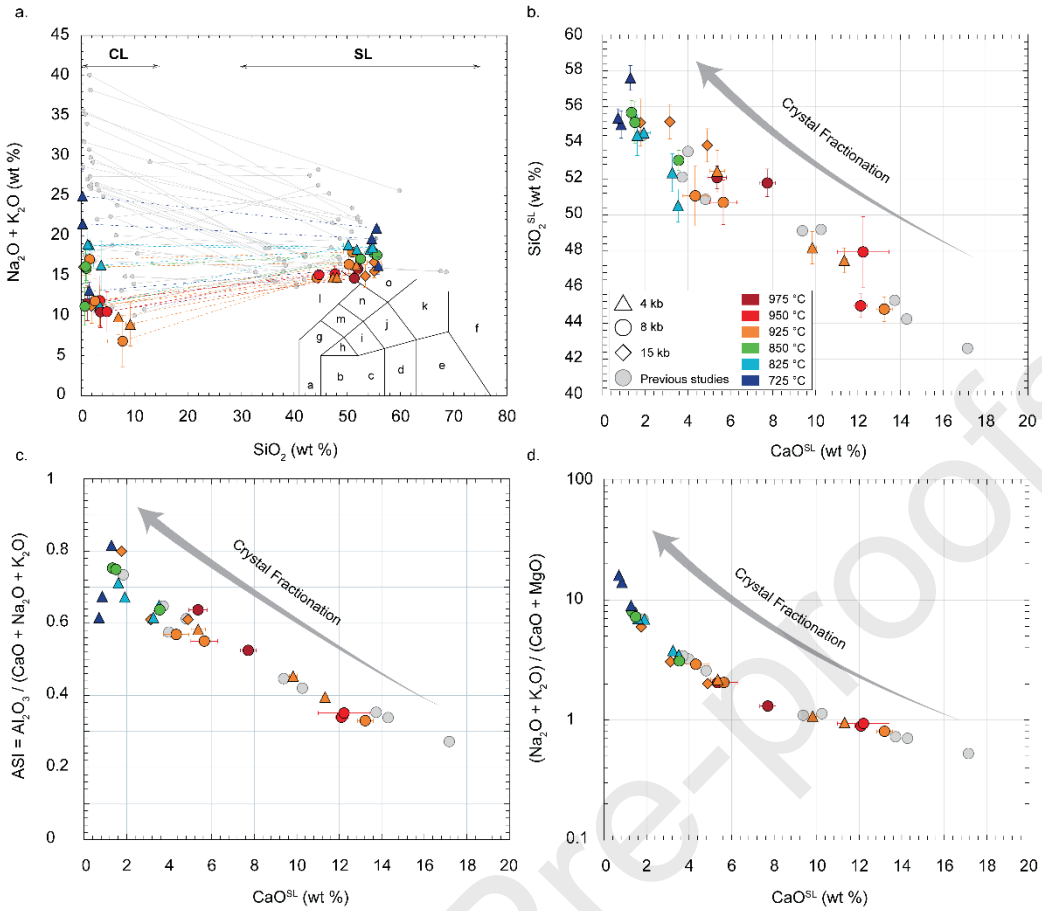

Fig. 2. Crystal fractionation effect on liquids composition. Major elements compositions of liquids from this study (coloured data symbols) and previous experimental investigations (grey dots; Hamilton et al., 1989; Veksler et al., 1998; Veksler et al., 2012; Martin et al., 2013). (a) Total alkali versus SiO_2 (TAS; (Le Bas et al., 1986) diagram of immiscible carbonate and silicate liquids (a: picro-basalt; b: basalt; c: basaltic andesite; d: andesite; e: dacite; f: rhyolite; g: tephri-basanite; h: trachy-basalt; i: basaltic trachy-andesite; j: trachy-andesite; k: trachyte; l: foïdite; m: phono-tephrite; n: tephri-phonolite; o: phonolite). The silicate liquid compositions are on a volatile-free basis. Each line connects a carbonate liquid (CL) coexisting at equilibrium with a silicate liquid (SL). Error bars indicate the standard deviation. Silica content (b), alumina saturation index (b) and alkaline/alkaline earth cations ratio (c) versus the CaO contents of the silicate melt. SiO_2 and CaO contents are in wt % on a volatile free basis, and the alumina saturation index and alkaline/alkaline earth cations ratio are in molar fractions. For (b) to (d), data from this study are compared to data from Kjarsgaard (1998; grey dots) which also experimented crystal fractionation.

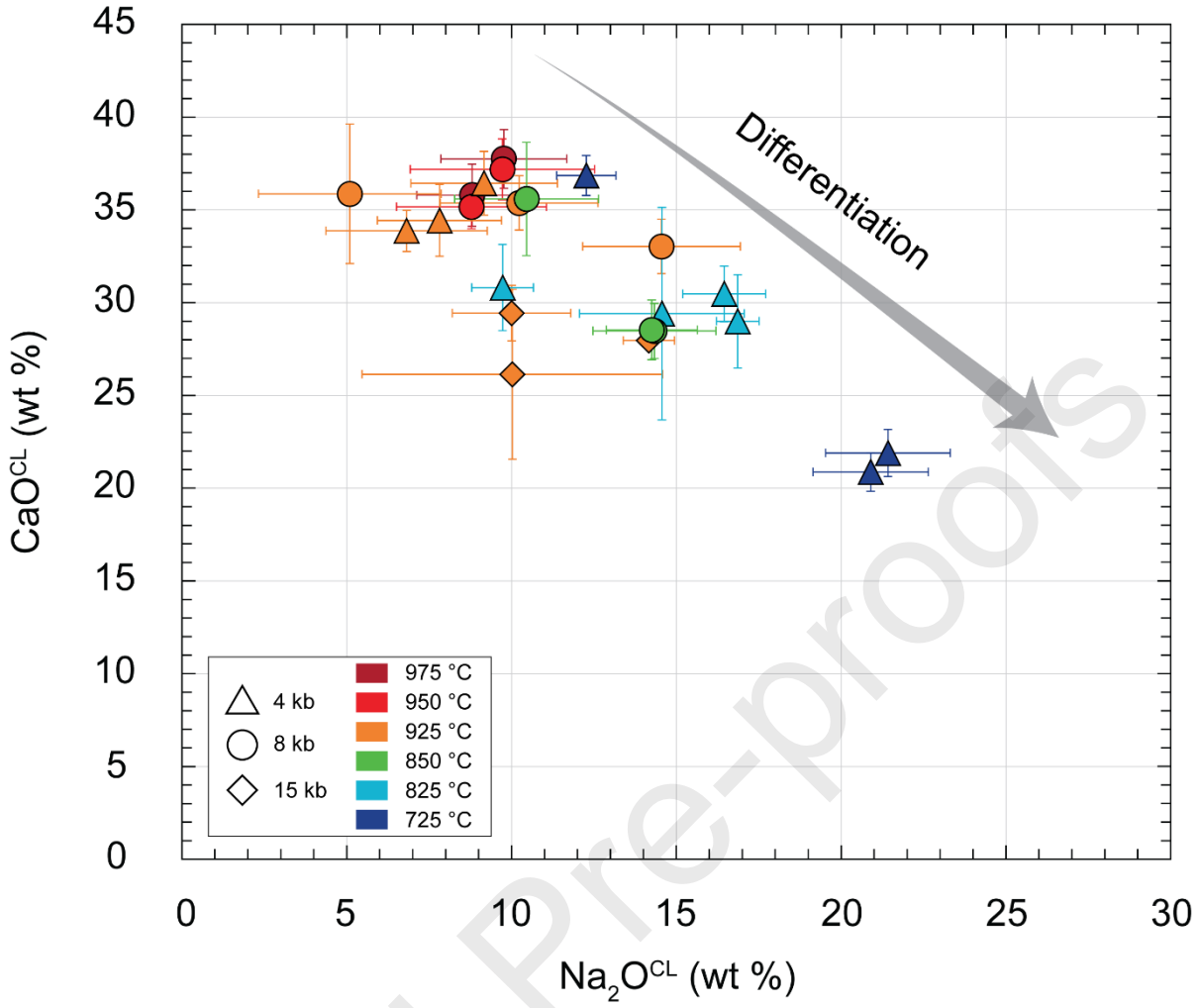

Fig. 3. Variation of carbonate liquid compositions during the differentiation. CaO contents versus the Na_2O contents of the carbonate liquids in wt%, for all P-T conditions. Carbonate liquids evolved from a Ca-rich pole towards a Na-rich pole along the differentiation. CL: carbonate liquid.

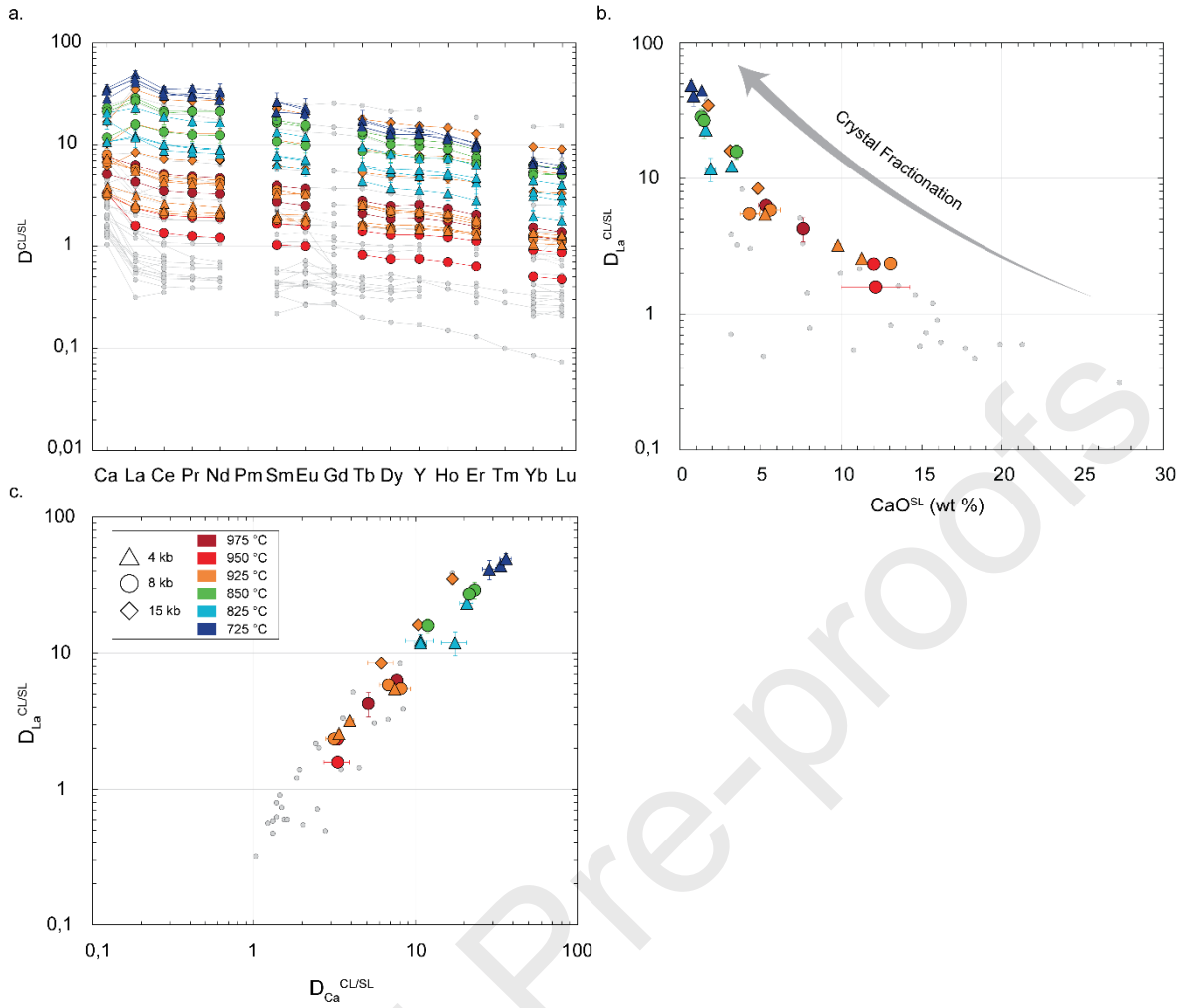

Fig. 4. REE behaviour between carbonate and silicate liquids. REE partition coefficients ($D_{REE}^{CL/SL}$) from this study and previous experimental investigations (grey dots; Hamilton et al., 1989; Veksler et al., 1998; Veksler et al., 2012; Martin et al., 2013). (a) Ca and REE partition coefficients measured between carbonate and silicate liquids. (c) and (d) La partition coefficients ($D_{La}^{CL/SL}$) respectively versus the wt% CaO in the silicate melts and Ca partition coefficients ($D_{Ca}^{CL/SL}$). CL: carbonate liquid; SL: silicate liquid.

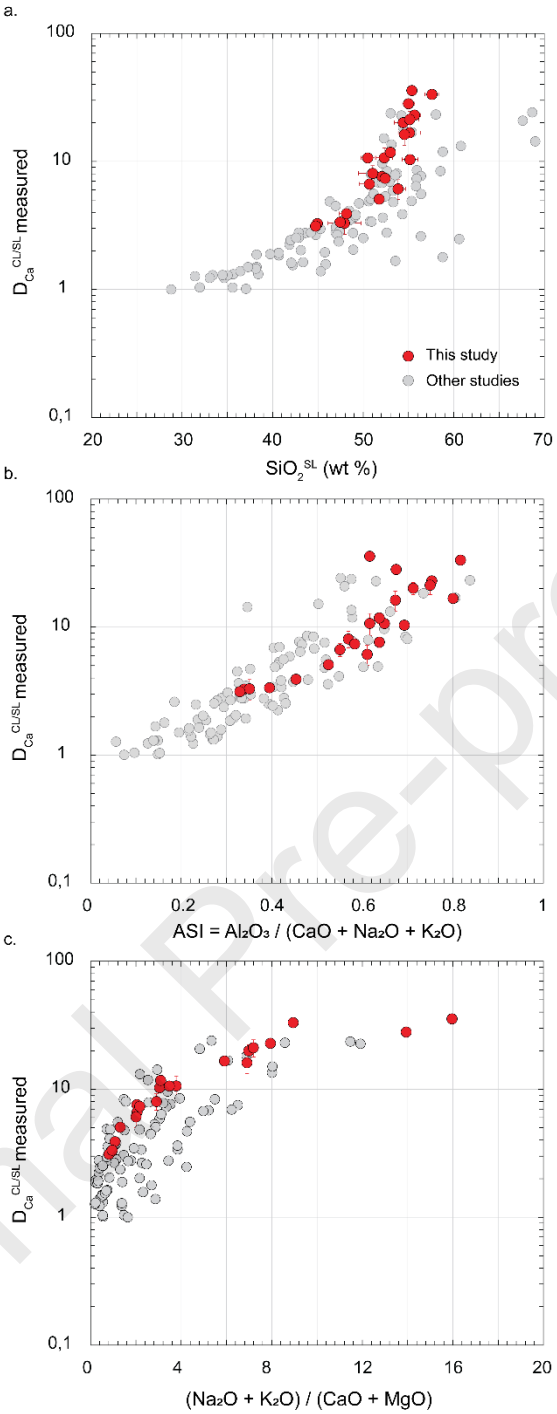

Fig. 5. Ca partitioning dependence on melt compositions. We represent the measured Ca partition coefficient ($D_{Ca}^{CL/SL}$) between carbonate and silicate melts, against three terms relative to the silicate melts composition used for the $D_{Ca}^{CL/SL}$ calibration: the silica content (a), the ASI (alumina saturation index) (b) and alkali/alkaline-earth cation ratio (c) for this study (red dots) and the experimental database used for the modelling (grey dots; Freestone and Hamilton, 1980; Hamilton et al., 1989; Kjarsgaard et al., 1995; Jones et al., 1995; Brooker, 1998; Kjarsgaard, 1998; Veksler et al., 1998; Veksler et al., 2012; Martin et al., 2012; Martin et al., 2013; Massuyeau et al., 2015). CL: carbonate liquid; SL: silicate liquid.

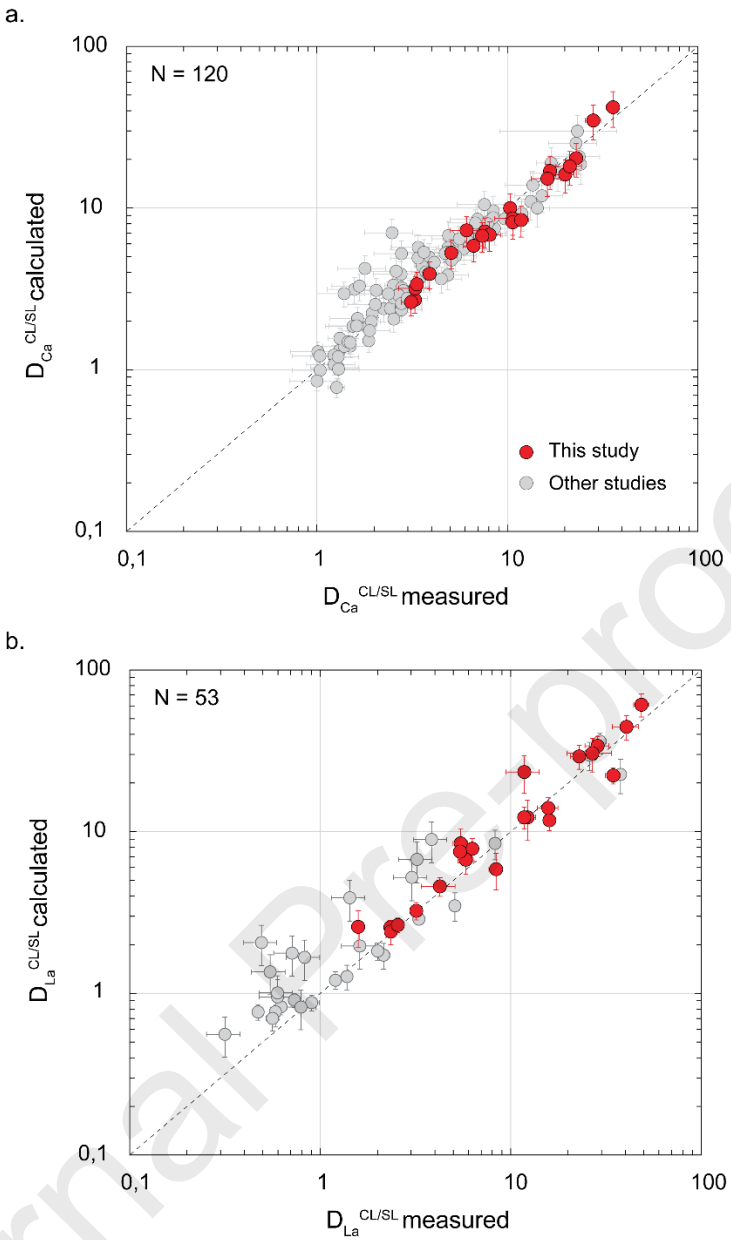

Fig. 6. Modelling for calcium and lanthanum partition coefficients between carbonate and silicate liquids. a. Modeled Ca partition coefficients between carbonate and silicate immiscible liquids ($D_{Ca}^{CL/SL}$ calculated) represented versus the experimentally measured Ca partition coefficients ($D_{Ca}^{CL/SL}$ measured), from this study (red dots) and the immiscibility database (grey dots; Tables 6 and 7a) used for the model (Freestone and Hamilton, 1980; Hamilton et al., 1989; Kjarsgaard et al., 1995; Jones et al., 1995; Brooker, 1998; Kjarsgaard, 1998; Veksler et al., 1998; Veksler et al., 2012; Martin et al., 2012; Martin et al., 2013; Massuyeau et al., 2015). b. Modeled La partition coefficients ($D_{La}^{CL/SL}$ calculated) as representative of other REE partitioning, against measured La partitioning ($D_{La}^{CL/SL}$ measured) parameterised from this study and other experimental studies (Hamilton et al., 1989; Veksler et al., 2012; Martin et al., 2013) on REE partitioning (Tables 6 and 7b). CL: carbonate liquid; SL: silicate liquid.

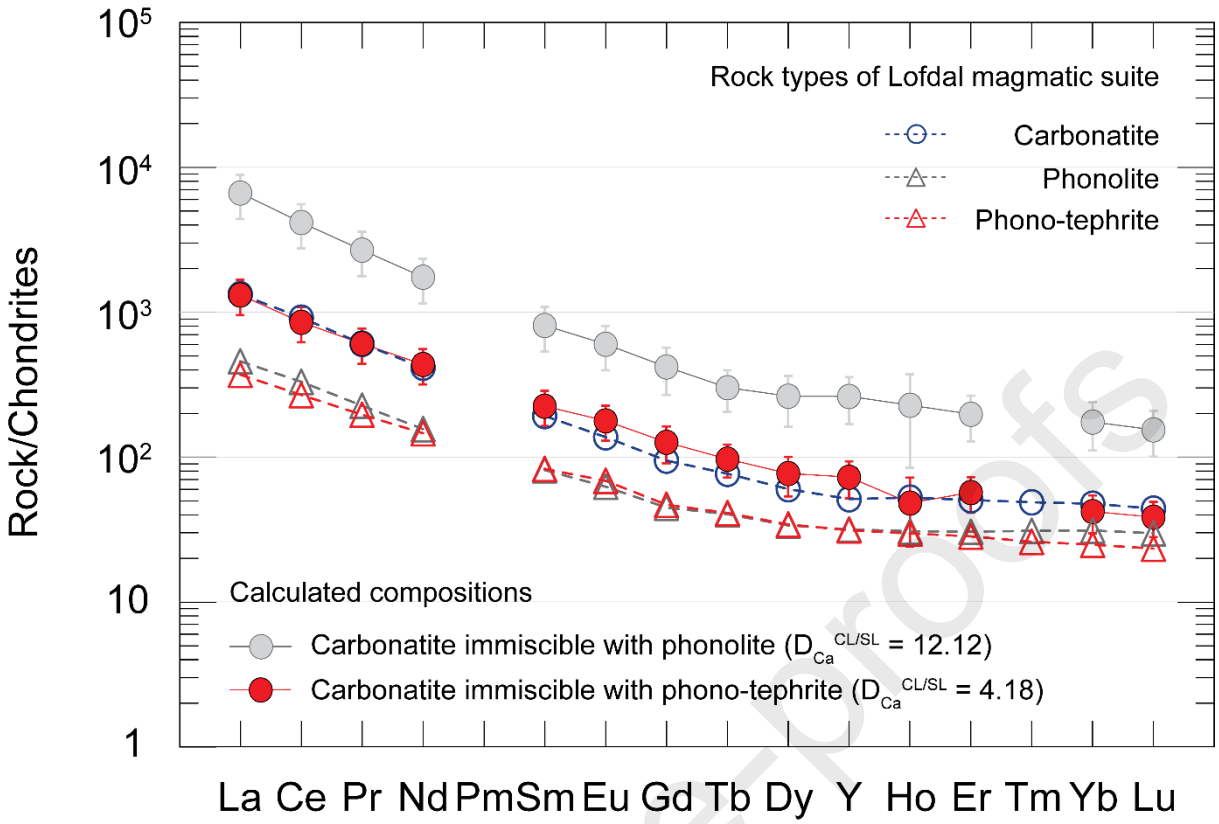

Fig. 7. Modelled carbonatite REE compositions compared to the natural carbonatite and silicate rock compositions of Lofdal in Namibia. Carbonatite REE contents are calculated here from phonolite (grey triangles) and phono-tephrite (red triangles) mean compositions of the Lofdal magmatic suite in Namibia (Bodeving et al., 2017) and normalised to chondrites (McDonough and Sun, 1995). The calculated carbonatite REE concentrations (filled circles) are compared to those of the natural carbonatite from this district (open blue circles; Bodeving et al., 2017). The error bars of the two compositions are estimated from the error propagation formalism detailed in the main text. Ca partition coefficients calculated from the first step of the modelling are indicate for both calculated carbonatite REE compositions in brackets.

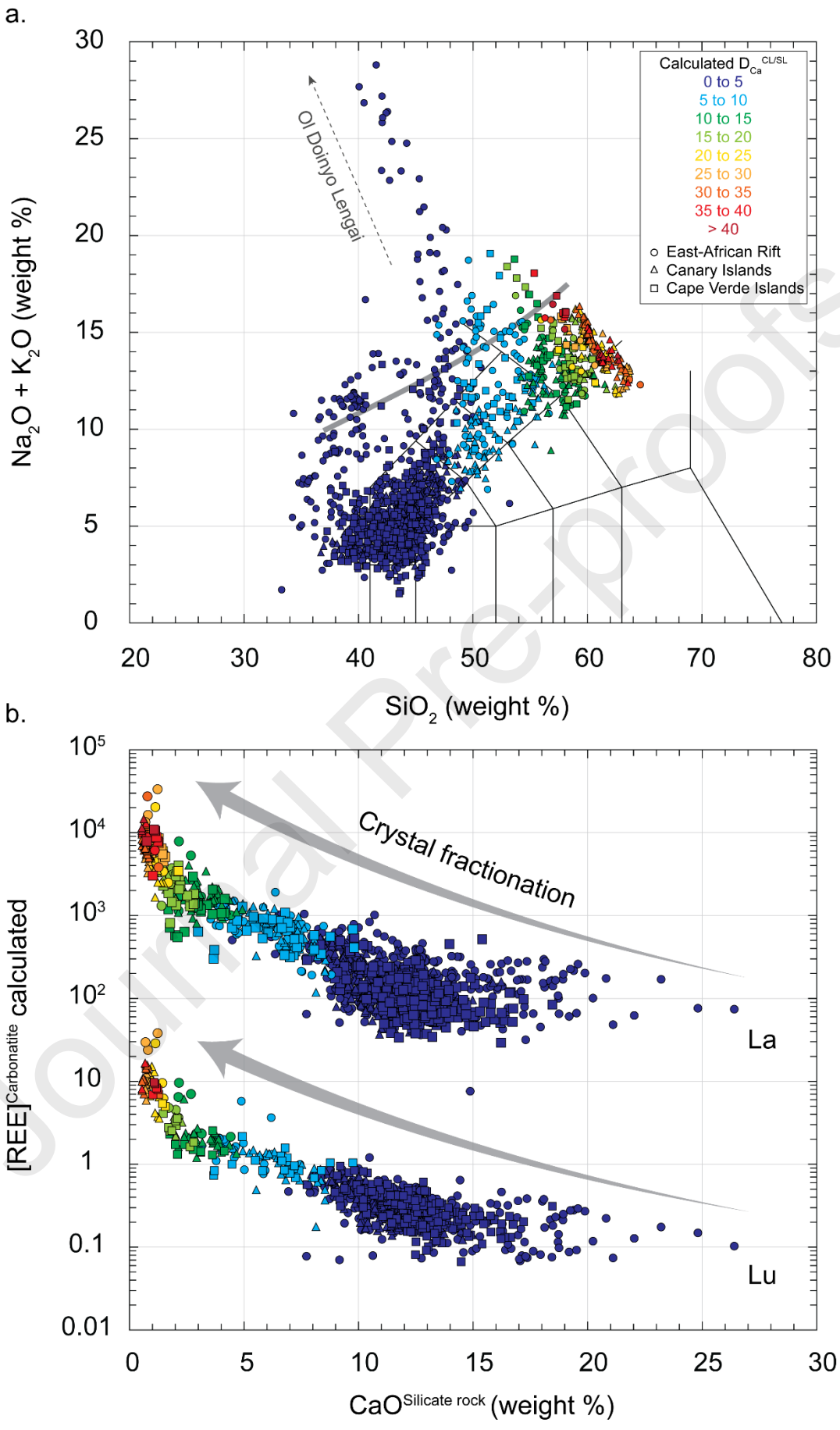

Fig. 8. Natural alkaline magmatic rocks from the East-African Rift and the Canary and Cape Verde Islands, and calculated composition of potential associated carbonatites. **a)** TAS diagram showing the composition of alkaline magmatic rocks (on a volatile-free basis) from the East-African Rift, the Canary Islands and the Cape Verde Islands: data from the GEOROC database and additional studies (De Moor et al., 2013; Mattsson et al., 2013; Mana et al., 2015). The colour gradient from blue to red indicates increasing values of $D_{Ca}^{CL/SL}$, calculated from the major element composition of each silicate rock, for the East-African Rift (circles), Canary Islands (triangles) and Cape Verde Islands (squares) settings. Data from the Ol Doinyo Lengai volcano in Tanzania (black arrow) follow a different trend of differentiation characterised by hyper-alkaline compositions (De Moor et al., 2013). The grey line correspond to the maximum extent of miscibility gap proposed by Schmidt and Weidendorfer (2018) which separate the field where immiscibility has been observed from the domain not investigated so far (Fig. A.4). **b)** Calculated La and Lu concentrations of potential carbonatites coexisting with alkaline magma compositions in (a), against the CaO contents (wt%) of the alkaline magmatic rocks from the three geological settings.

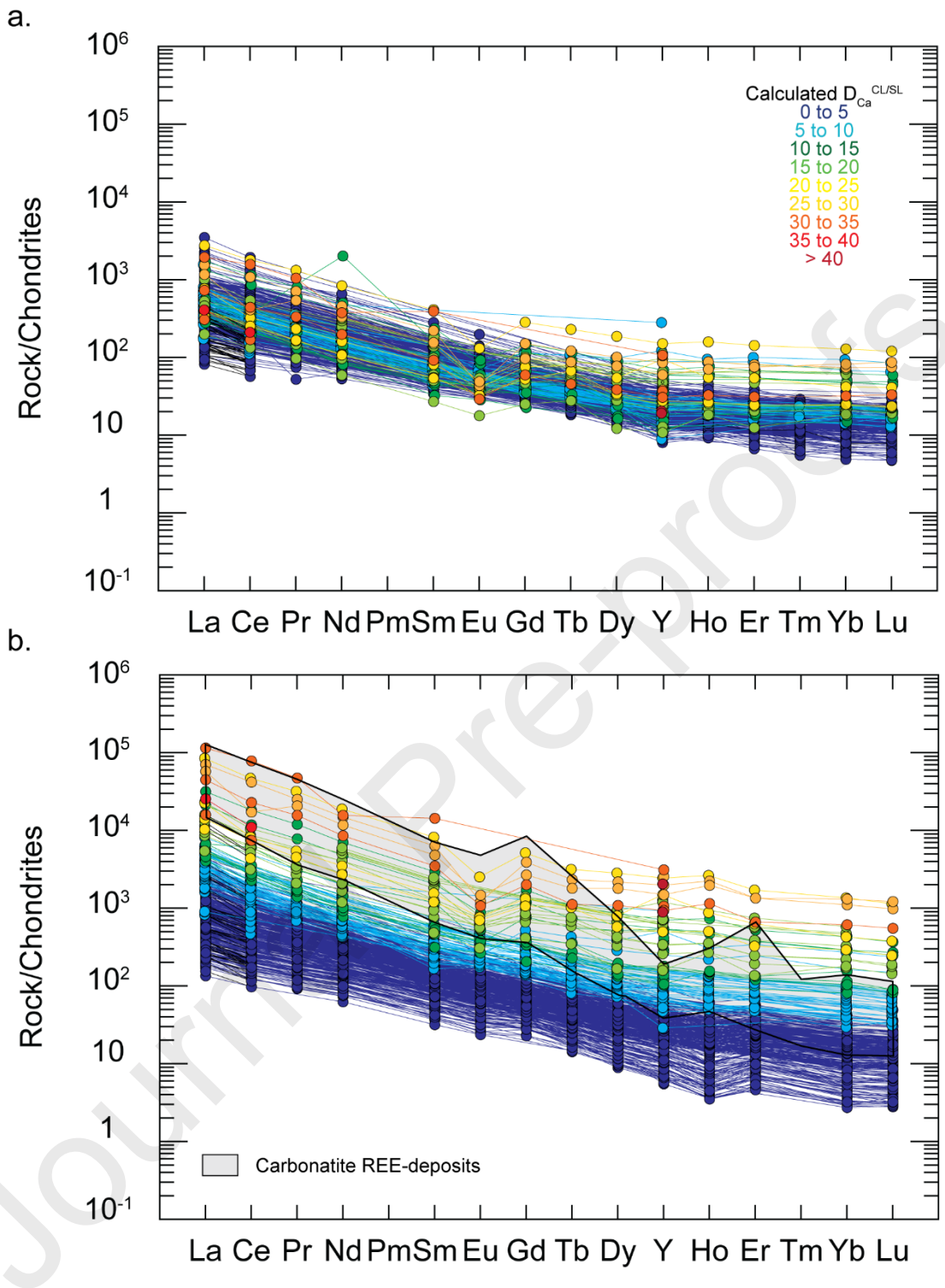

Fig. 9. Alkaline magmatic rocks from the East African Rift and calculated carbonatite compositions normalised to chondrite. (a) Changes in the REE contents of alkaline magmatic rocks from the East African Rift across differentiation. The East-African Rift silicate magmatic rocks used to calculate carbonatite REE contents of Fig. 8 are normalised to chondrites (McDonough and Sun, 1995). The calculated Ca partition coefficient ($D_{Ca}^{CL/SL}$ calculated) is represented for each magmatic composition

by a colour gradient (data from GEOROC; De Moor et al., 2013; Mattsson et al., 2013; Mana et al., 2015). (b) Calculated carbonatite REE compositions normalised to chondrites. REE contents of carbonatites are calculated from the alkaline silicate magma compositions and are normalised to chondrite (McDonough and Sun, 1995). The anomalies in some chondrite-normalised REE profiles reflect anomalies of natural silicate rocks compositions. The profiles are characterized by a strong enrichment in LREE and a relatively slight flat distribution of HREE. The grey field represents the compositions of carbonatite REE deposits currently mined: Bayan Obo, Mianing deposits and Mountain Pass (from Verplanck et al., 2016).

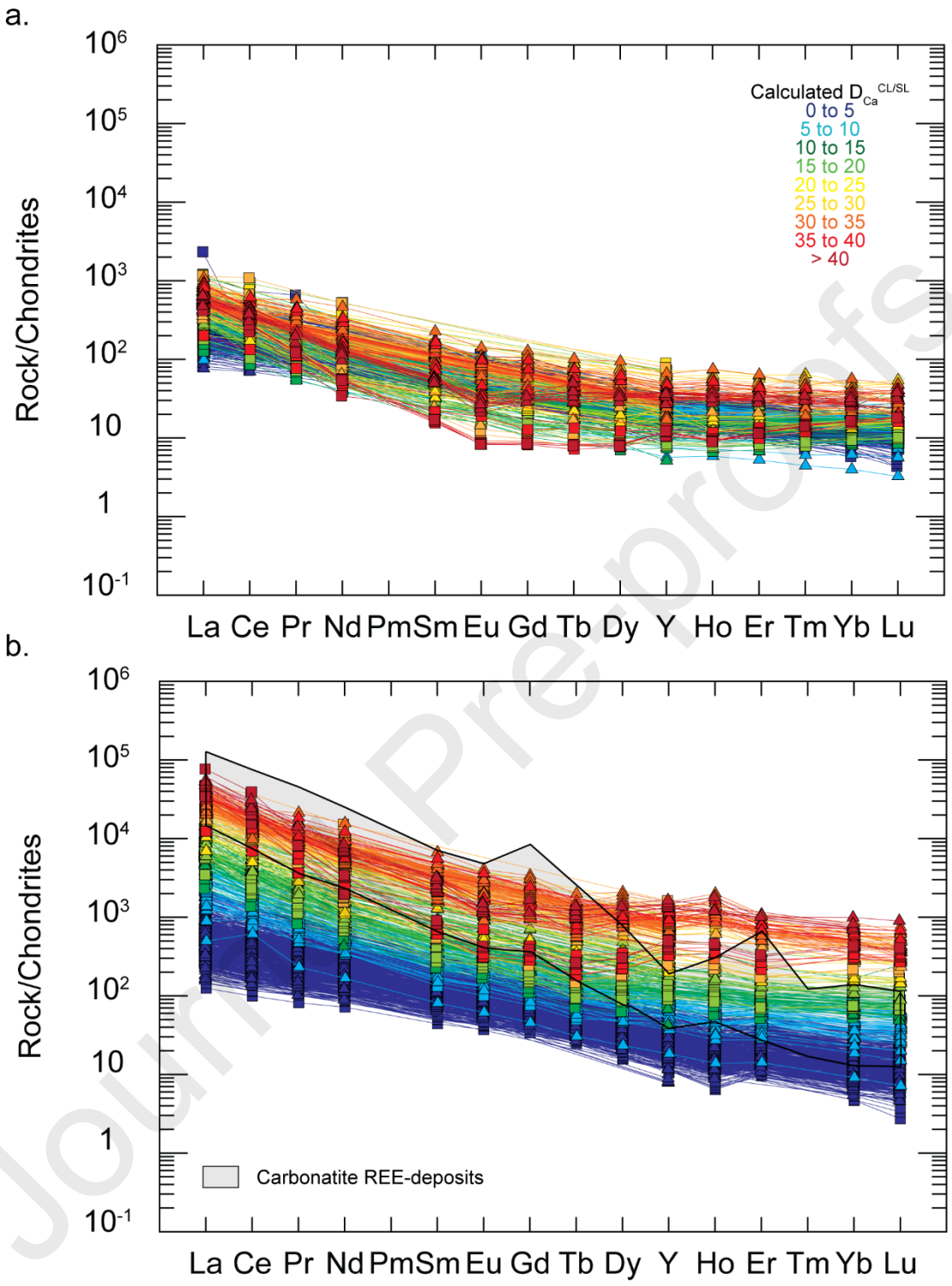

Fig. 10. Alkaline magmatic rocks from the Canary and Cape Verde Islands, and calculated carbonatite compositions normalised to chondrite. (a) Changes in the REE contents of alkaline magmatic rocks from the Canary (triangles) and Cape Verde Islands (squares) across differentiation (data from GEOROC database). The silicate magmatic rocks used to calculate carbonatite REE contents of Fig. 8 are normalised to chondrites (McDonough and Sun, 1995) for boths settings. The colour gradient represent

the calculated Ca partition coefficient ($D_{Ca}^{CL/SL}$ calculated) for each magmatic rocks by a. (b) Calculated carbonatite REE compositions normalised to chondrites, for the Canary and Cape Verde Islands. Carbonatite REE compositions are calculated from the alkaline silicate magmas shown in Fig. 8 and normalised to chondrite (McDonough and Sun, 1995). The chondrite-normalised REE profiles are also characterised by a strong enrichment in LREE and a relatively slight flat distribution of HREE. The grey field represents the compositions of carbonatite REE deposits currently mined: Bayan Obo, Mianing deposits and Mountain Pass (from Verplanck et al., 2016).

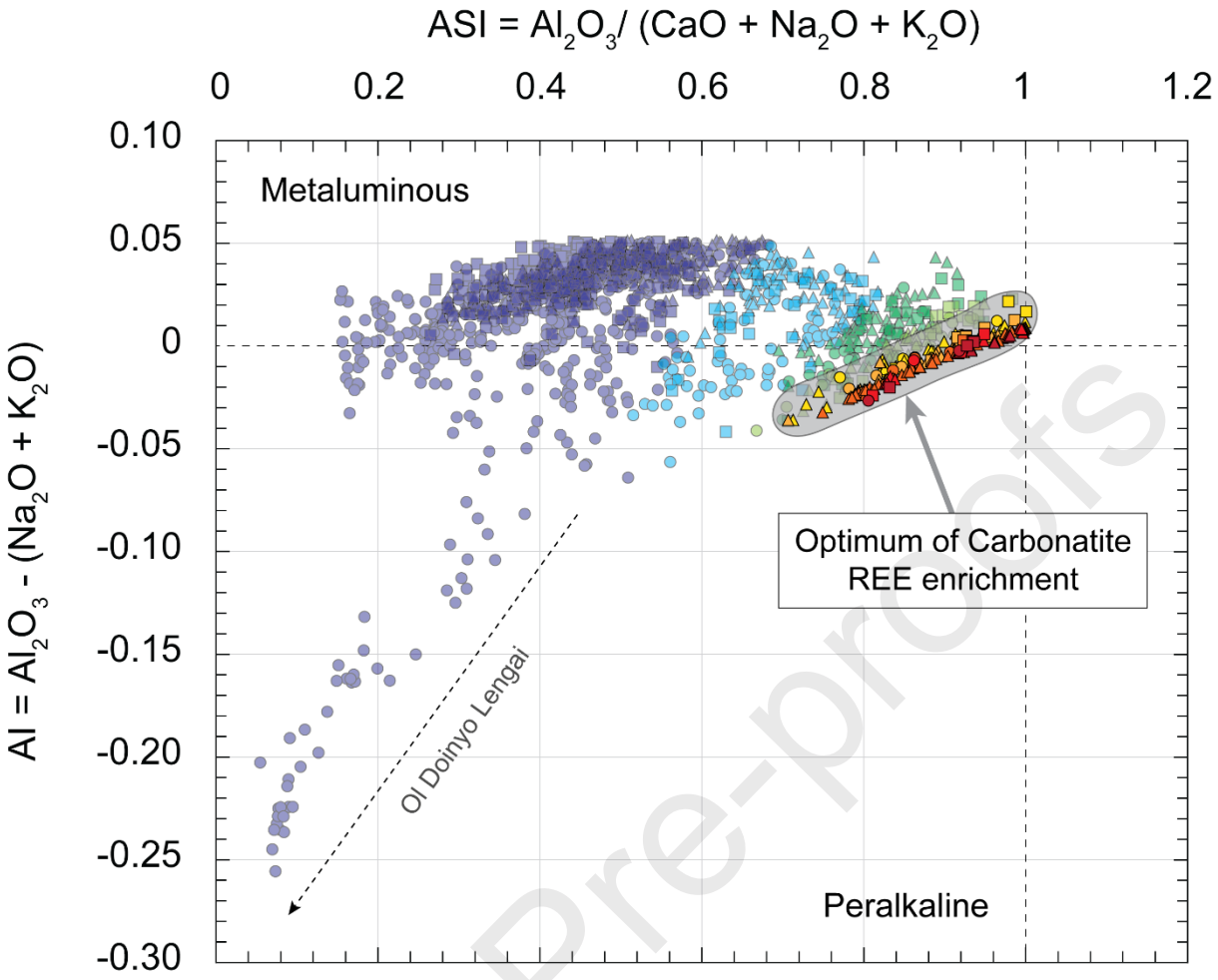

Fig. 11. Optimum of carbonatite REE enrichment along the alkaline magma differentiation course, for the East African Rift and Canary and Cape Verde Islands. The alkalinity index (AI = AL_2O_3-(Na_2O+K_2O)) for all the alkaline magmatic rocks of the three settings from Fig.8-9-10 is represented against their alumina saturation index (ASI = Al_2O_3 / (CaO+Na_2O+K_2O)). Both index are calculated in molar fractions. The calculated Ca partition coefficient ($D_{Ca}^{CL/SL}$ calculated) is represented for each magmatic compositions by a colour gradient. The optimum of carbonatite REE enrichment correspond to phonolitic / phono-trachytic compositions ($D_{Ca}^{CL/SL} > 20$), at the boundary between peralkaline and metaluminous domains (grey field). The hyper-alkaline rocks from the Ol Doinyo Lengai volcano (black arrow) which present a strong peralkalinity, are far from this optimum.